



Continuum model study of optical absorption by hybridized moiré excitons in transition metal dichalcogenide heterobilayers

Yao-Wen Chang *Physics Division, National Center for Theoretical Sciences, National Taiwan University, Taipei 10617, Taiwan* (Received 27 April 2023; revised 27 September 2023; accepted 5 October 2023; published 20 October 2023)

We propose a continuum model for the theoretical study of hybridized moiré excitons in transition-metal dichalcogenides heterobilayers, and we use a variational method to solve the exciton wave function and calculate the optical absorption spectrum. The exciton continuum model is built by the charge continuum model for electrons and holes in moiré superlattices, thereby preserving the moiré periodicity and lattice symmetry from the charge continuum model. The momentum-space shift of interlayer electron-hole distribution is included, and thus the indirect nature of interlayer excitons is described. The spin and valley degrees of freedom and related interactions are omitted, except for the spin-orbit energy splitting of A and B excitons. This continuum model is applied to the simulation of optical absorption by hybridized moiré excitons in WSe_2/WS_2 and $\text{MoSe}_2/\text{WS}_2$ heterobilayers. Twist-angle and electric-field dependencies of absorption spectra are studied. Calculated spectra are compared with experimental observations in the literature, and correspondences of signatures are found. The deficiency and the potential of the present model are discussed.

DOI: [10.1103/PhysRevB.108.155424](https://doi.org/10.1103/PhysRevB.108.155424)

I. INTRODUCTION

Two-dimensional (2D) semiconducting materials, such as transition-metal dichalcogenides (TMDCs), are promising to be applied in future photonic and optoelectronic devices [1–3]. Excitonic effects are critical for deciding the optical properties of 2D semiconductors due to the reduction of dielectric screening and the enhancement of quantum confinement [4,5]. Recently, moiré heterostructures stacked by 2D semiconducting materials with twisted angles or lattice mismatches have been predicted theoretically and synthesized experimentally. Emergent physical phenomena related to the additional moiré degree of freedom have been observed and discussed [6–10]. Exciton physics in this system is also studied. Excitons in moiré heterostructures are modulated by interlayer charge-transfer couplings and moiré periodic potentials, which are formed by local atomic registry changes [11–25]. Optical properties of excitons in 2D heterostructures can be tuned by this additional moiré degree of freedom. The applications of 2D layered materials are widened by this new tunability.

An exciton is an electron-hole pair bound by Coulomb attraction [4,5]. Excitonic signatures can be found in direct-gap semiconductors and detected by optical spectroscopy. For multilayer materials, excitons can be sorted as intralayer excitons, where the electron and the hole are at the same layer, and interlayer excitons, where the electron and the hole are at different layers. In TMDC heterobilayers with type-II band alignment, the lowest-energy excitation is contributed from the interlayer exciton, which has a small electron-hole wave function overlap [12,17]. Therefore, interlayer valence-to-conduction band transition has a low oscillator strength, and thus interlayer-exciton signatures are difficult to be observed in absorption spectra. While there is no direct interlayer

exciton transition in TMDC heterobilayers, electron transfer between conduction bands on each layer or hole transfer between valence bands on each layer could occur. The charge transfer contributes to the formation of interlayer excitons. In some situations, such as by applying a perpendicularly electric field to tune the band gaps, the difference between the optical transition energy of interlayer excitons and the transition energy of intralayer excitons can be at the same scale as the interlayer charge-transfer coupling. Hybridization between interlayer excitons and intralayer excitons forms hybrid excitons. These hybrid excitons borrow the oscillator strength from the intralayer exciton, and thus they can be observed in absorption spectra [26–28].

With the additional moiré degree of freedom in TMDC heterobilayers, excitons become trapped by the moiré potential, and the translational symmetry of the center-of-mass (COM) motion of excitons becomes broken. The interlayer charge-transfer coupling should also follow the same moiré periodicity with the potential. If the physical properties of an exciton are decided or strongly affected by this moiré degree of freedom, the exciton can be called a moiré exciton [22–24]. Various theoretical methods have been proposed and applied to the research of moiré excitons [29–44]. An effective continuum model which describes the COM motion of an exciton being modulated by a periodic potential as the moiré potential has been widely used to find exciton band structures and exciton wave functions [30–32]. For more generalized continuum models [34,39,41,42], the interlayer charge-transfer coupling is included. However, these models only describe the COM motion of moiré excitons, such that the effect of moiré periodicity on the internal motion of excitons has not been discussed. A more sophisticated method is to apply atomistic calculation with density-functional theory (DFT) to simulate the hybridized moiré excitons [36–38,43]. However, since the

unit cell for moiré superlattices is usually quite large, the atomistic approach with DFT is expensive computationally. A method to model impartially and simulate efficiently hybridized moiré excitons is still lacking. It is the gap we intend to fill in this work.

In this article, we provide an improved version of the exciton continuum model to study the hybridized moiré excitons in TMDC heterobilayers with lattice mismatches and small twist angles. The exciton continuum model is written down based on four conditions. First, the exciton continuum model is built by the charge continuum model for electrons and holes in moiré superlattices, thereby preserving the moiré periodicity and lattice symmetry from the charge continuum model. Second, the momentum-space shift of interlayer electron-hole distribution is included, and thus the indirect nature of interlayer excitons is described. Third, the spin and valley degrees of freedom and related interactions are omitted, except for the spin-orbit energy splitting of A and B excitons. Forth, in long moiré-wavelength and zero charge-transfer-coupling limits, the exciton model and the optical absorption formula can be reduced to the counterparts of an isolated exciton. A variational method using Slater-type orbitals (STOs) as the basis function is applied to the numerical solution of the exciton continuum model. Optical absorption by hybridized moiré excitons is studied with varying twist angles in small degrees and varying out-of-plane electric fields to tune the band-edge energy. Twist-angle-dependent and electric-field-dependent absorption spectra of WSe_2/WS_2 and $\text{MoSe}_2/\text{WS}_2$ heterobilayers are simulated. A good correspondence between the calculated spectra from this work and the experimentally observed spectra from the literature is achieved. In Sec. II, the exciton continuum model is derived based on the moiré periodicity and the charge continuum model. The methods to solve the exciton wave function and the optical transition amplitude are also introduced. In Sec. III, the model is applied to the simulation of twist-angle-dependent and electric-field-dependent absorption spectra of WSe_2/WS_2 and $\text{MoSe}_2/\text{WS}_2$ heterobilayers. In Sec. IV, the applications and improvements of this model in the future study are discussed, and the conclusion is given. In Appendix B, matrix elements of the exciton continuum model spanned by STO and plane-wave basis functions are given.

II. THEORY

In this section, the continuum model for hybridized moiré excitons in TMDC heterobilayers is derived, and the method to calculate the exciton wave function and the optical spectrum is given. In Sec. II A, the geometry of moiré superlattices and reciprocal lattices is illustrated, and the concept of moiré Brillouin zone (MBZ) is introduced. In Sec. II B, the charge continuum model and the many-body formulation are introduced. The expression of screened Coulomb interaction in the many-body Hamiltonian is also discussed. In Sec. II C, the exciton continuum model is derived through the many-body formulation. A transformation from electron and hole position coordinates to exciton COM and internal coordinates is applied to the continuum model. In Sec. II D, the variational

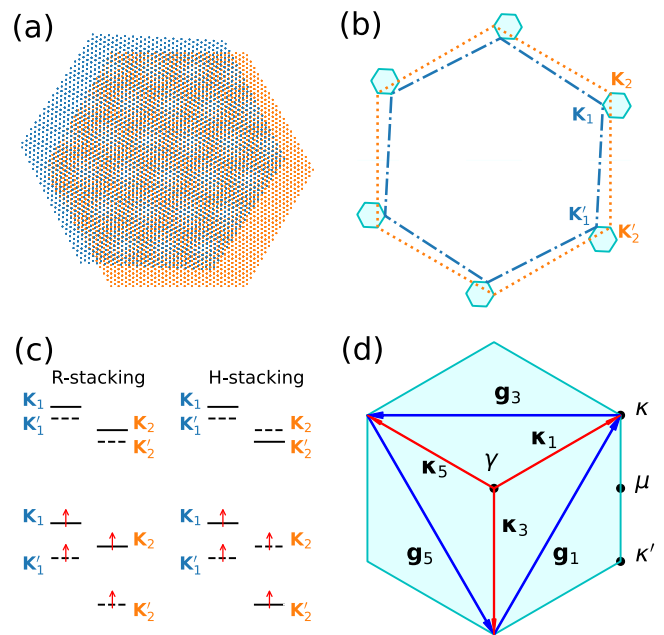


FIG. 1. (a) Schematic plot of the R-stacked heterobilayer with lattice mismatch $\delta = 0.1$ and a twisted angle $\theta = 3^\circ$. (b) Schematic plot of the Brillouin zone of the top monolayer (inside blue dash-dotted hexagonal) and the Brillouin zone of the bottom monolayer (inside orange dot hexagonal) of the R-stacked heterobilayer. The filled zone is the MBZ of heterobilayers. (c) Energy-level diagram of band edges at the top monolayer $\mathbf{K}_1, \mathbf{K}'_1$ and band edges at the bottom monolayer $\mathbf{K}_2, \mathbf{K}'_2$ in R-stacked and H-stacked heterobilayers. (d) A closer look at the MBZ of the heterobilayer and high-symmetry points.

method is introduced to solve the exciton wave function. In Sec. II E, the method to calculate the optical absorption spectrum is discussed.

A. Moiré superlattice and moiré Brillouin zone

There are two types of stacking for TMDC heterobilayers: R-stacking and H-stacking. R-stacked TMDC heterobilayers are stacking of two triangular lattices with near 0° rotation and H-stacked TMDC heterobilayers are stacking with near 60° rotation [21]. Small twist-angle variants straying from 0° and 60° rotations can still be considered as R-stacked and H-stacked heterobilayers. Schematic plots of the moiré superlattice and MBZ of the R-stacked heterobilayer are illustrated in Figs. 1(a) and 1(b). The lattice constant of the moiré superlattice a_M as a function of twist angle θ and the lattice mismatch $\delta = |a'_0 - a_0|/a_0$, with a_0, a'_0 the lattice constants for the atomistic lattices, is given by [6,9]

$$a_M = \frac{(1 + \delta)a_0}{\sqrt{2(1 + \delta)(1 - \cos \theta) + \delta^2}}. \quad (1)$$

The MBZ is built by the difference between reciprocal vectors in the Brillouin zone of the top monolayer (inside blue dash-dot hexagonal) and the Brillouin zone of the bottom monolayer (inside orange dot hexagonal), as illustrated in Fig. 1(b). The moiré superlattice can be considered a triangular lattice with the unit cell containing

local geometry. The primitive vectors of the moiré superlattice can be defined as $\mathbf{a}_1 = a_M[(\sqrt{3}/2)\mathbf{e}_x + (1/2)\mathbf{e}_y]$, $\mathbf{a}_2 = a_M[(-\sqrt{3}/2)\mathbf{e}_x + (1/2)\mathbf{e}_y]$. For the moiré reciprocal lattice, the reciprocal primitive vectors can be defined by $\mathbf{g}_i \cdot \mathbf{a}_j = 2\pi\delta_{ij}$ for $i, j = 1, 2$ and found to be $\mathbf{g}_1 = \sqrt{3}k_M[(1/2)\mathbf{e}_x + (\sqrt{3}/2)\mathbf{e}_y]$, $\mathbf{g}_2 = \sqrt{3}k_M[(-1/2)\mathbf{e}_x + (\sqrt{3}/2)\mathbf{e}_y]$, with $k_M = 4\pi/(3a_M)$. A set of reciprocal primitive vectors can be defined as $\mathbf{g}_j = \sqrt{3}k_M[\mathbf{e}_x \cos(j\pi/3) + \mathbf{e}_y \sin(j\pi/3)]$, with $j = 1, 2, \dots, 6$. The vector connects between κ and γ is given by $\boldsymbol{\kappa}_1 = (2\mathbf{g}_1 - \mathbf{g}_2)/3$ and the vector connects between κ' and γ is given by $\boldsymbol{\kappa}_2 = (\mathbf{g}_1 - 2\mathbf{g}_2)/3$. These two vectors $\boldsymbol{\kappa}_1$ and $\boldsymbol{\kappa}_2$ can be assigned as reciprocal basis vectors. A set of reciprocal basis vectors can be defined as $\boldsymbol{\kappa}_j = k_M[\mathbf{e}_x \cos(\pi/6 - j\pi/3) + \mathbf{e}_y \sin(\pi/6 - j\pi/3)]$, with $j = 1, 2, \dots, 6$. Part of the reciprocal primitive and basis vectors are shown in Fig. 1(d).

Energy-level diagrams of band edges on different layers with the same spin index on R-stacked and H-stacked heterobilayers are illustrated in Fig. 1(c) [12]. Spin-orbit coupling–induced (SOC-induced) energy-level splittings occur in both conduction bands and valence bands of both layers. Due to the intrinsic spin-valley locking of TMDCs, the \mathbf{K} and \mathbf{K}' valleys with the same spin index have different band-edge energies. As illustrated in Fig. 1(b), interlayer tunneling only occurs among energy levels with the same types of lines (solid line or dashed line). Optical transition is only allowed between valence and conduction bands at the same valley ($\mathbf{K}_1, \mathbf{K}'_1, \mathbf{K}_2, \mathbf{K}'_2$). Via this diagram and effective-mass-model parameters for TMDC monolayers, band-edge energies for different intralayer or interlayer excitons in R-stacked or H-stacked heterobilayers can be evaluated.

B. Charge continuum model

The many-body Hamiltonian for electrons and holes in moiré superlattices including the electron-hole attraction is given by

$$\begin{aligned} \hat{H} = & \sum_{\mathbf{k}\mathbf{k}',l,l'} [\hat{c}_{l,\mathbf{k}}^\dagger \tilde{H}_{e,l,l'}(\mathbf{k}, \mathbf{k}') \hat{c}_{l,\mathbf{k}'} + \hat{d}_{l,\mathbf{k}}^\dagger \tilde{H}_{h,l,l'}(\mathbf{k}, \mathbf{k}') \hat{d}_{l,\mathbf{k}'}] \\ & + \frac{1}{2S} \sum_{l,l',\mathbf{q}} \tilde{W}_{ll'}(\mathbf{q}) (\hat{\rho}_{e,l,\mathbf{q}} \hat{\rho}_{e,l',-\mathbf{q}} + \hat{\rho}_{h,l,\mathbf{q}} \hat{\rho}_{h,l',-\mathbf{q}}) \\ & - \frac{1}{S} \sum_{l,l',\mathbf{q}} \tilde{W}_{ll'}(\mathbf{q}) \hat{\rho}_{e,l,\mathbf{q}} \hat{\rho}_{h,l',-\mathbf{q}}, \end{aligned} \quad (2)$$

where $\hat{c}_{l,\mathbf{k}}^\dagger$ ($\hat{c}_{l,\mathbf{k}}$) is the electron creation (annihilation) operator at layer l with wave vector \mathbf{k} , $\hat{d}_{l,\mathbf{k}}^\dagger$ ($\hat{d}_{l,\mathbf{k}}$) is the hole creation (annihilation) operator, $\tilde{H}_{c,l,l'}(\mathbf{k}, \mathbf{k}')$ is the charge Hamiltonian with $c = \{e, h\}$ the charge index indicating electrons and holes, $\hat{\rho}_{e,l,\mathbf{q}} = \sum_{\mathbf{k}} \hat{c}_{l,\mathbf{k}+\mathbf{q}}^\dagger \hat{c}_{l,\mathbf{k}}$ is the electron-density operator, $\hat{\rho}_{h,l,\mathbf{q}} = \sum_{\mathbf{k}} \hat{d}_{l,\mathbf{k}+\mathbf{q}}^\dagger \hat{d}_{l,\mathbf{k}}$ is the hole-density operator, S is the area of the lattice, and $\tilde{W}_{ll'}(\mathbf{q}) = \int e^{-i\mathbf{q}\cdot\mathbf{r}} W_{ll'}(\mathbf{r}) d^2r$ is the screened Coulomb interaction. Note that we have ignored the spin and valley degrees of freedom in this many-body Hamiltonian.

The charge Hamiltonian in real space is related to the charge Hamiltonian in k space through the Fourier transform

$\tilde{H}_{c,l,l'}(\mathbf{k}, \mathbf{k}') = \int e^{-i(\mathbf{k}-\mathbf{k}')\cdot\mathbf{r}} H_{c,l,l'}(\mathbf{r}) d^2r$ and is given by [45]

$$H_c(\mathbf{r}) = \begin{pmatrix} h_{c,1}(\mathbf{r}) & t_c(\mathbf{r}) \\ t_c^*(\mathbf{r}) & h_{c,2}(\mathbf{r}) \end{pmatrix}, \quad (3)$$

where $h_{c,l}(\mathbf{r})$ is the layer-charge Hamiltonian of the l th layer and $t_e(\mathbf{r})$, $t_h(\mathbf{r})$ is the interlayer tunneling coupling. The layer-charge Hamiltonian is given by

$$h_{c,l}(\mathbf{r}) = \epsilon_{c,l} - z_c U_l(\mathbf{r}) + \frac{|\mathbf{p} + z_c \boldsymbol{\kappa}_l|^2}{2m_{c,l}}, \quad (4)$$

where $\mathbf{p} = -i\nabla$ is the momentum operator of the charge particle, $z_e = -$ and $z_h = +$ are the charge parity, $\epsilon_{c,l}$ is the band-edge energy, $m_{c,l}$ is the charge mass at layer l , $U_l(\mathbf{r})$ is the moiré potential. The moiré potential is given by the harmonic-function form

$$U_l(\mathbf{r}) = 2V_l \sum_{j=1,3,5} \cos(\mathbf{g}_j \cdot \mathbf{r} + \psi_l), \quad (5)$$

and the interlayer tunneling couplings are given by

$$t_e(\mathbf{r}) = w_e (1 + e^{i\mathbf{g}_1 \cdot \mathbf{r}} + e^{i\mathbf{g}_2 \cdot \mathbf{r}}), \quad (6)$$

$$t_h(\mathbf{r}) = w_h (1 + e^{-i\mathbf{g}_1 \cdot \mathbf{r}} + e^{-i\mathbf{g}_2 \cdot \mathbf{r}}), \quad (7)$$

where V_l is the moiré potential depth at layer l , ψ_l is the phase angle, and w_e (w_h) are the electron (hole) interlayer-tunneling coupling strength. In this work, the phase angle is always chosen to be $\psi_l = -(-1)^l \pi/2$, such that the moiré potential can be rewritten as $U_l(\mathbf{r}) = 2V_l (-1)^l \sum_{j=1,3,5} \sin(\mathbf{g}_j \cdot \mathbf{r})$.

The screened Coulomb potential is described by a modified Rytova-Keldysh potential [46,47], which is written as

$$\tilde{W}_{ll'}(\mathbf{q}) = \frac{2\pi}{\epsilon_{ll'}(q)q}, \quad (8)$$

where $\epsilon_{ll'}(q)$ is the bilayer dielectric function determined by intrinsic properties of heterobilayers. While there are many formulations for the bilayer dielectric function [33,35,48–51], here we use a simple form derived in Appendix A. The intralayer and interlayer dielectric functions are given by

$$\epsilon_{11}(q) = \frac{\kappa_0 \epsilon_{12}(q)}{\left(\frac{\kappa_1 + \kappa_0}{2} + r_2 q\right) e^{qd} - \left(\frac{\kappa_1 - \kappa_0}{2} + r_2 q\right) e^{-qd}}, \quad (9)$$

$$\epsilon_{22}(q) = \frac{\kappa_0 \epsilon_{12}(q)}{\left(\frac{\kappa_1 + \kappa_0}{2} + r_1 q\right) e^{qd} - \left(\frac{\kappa_1 - \kappa_0}{2} + r_1 q\right) e^{-qd}}, \quad (10)$$

$$\begin{aligned} \epsilon_{12}(q) = & \left(\frac{\kappa_1 + \kappa_0}{2} + r_1 q\right) \left(\frac{\kappa_1 + \kappa_0}{2} + r_2 q\right) \frac{e^{qd}}{\kappa_0} \\ & - \left(\frac{\kappa_1 - \kappa_0}{2} + r_1 q\right) \left(\frac{\kappa_1 - \kappa_0}{2} + r_2 q\right) \frac{e^{-qd}}{\kappa_0}, \end{aligned} \quad (11)$$

and $\epsilon_{21}(q) = \epsilon_{12}(q)$, where κ_1 is the dielectric constant outside the bilayer, κ_0 is the dielectric constant inside the bilayer, r_l is the screening length on the l th layer, and d is the interlayer distance.

C. Exciton continuum model

An exciton state is assumed to be written as $|X_I\rangle = X_I^\dagger |0\rangle$, where

$$X_I^\dagger = \sum_{l_e, l_h} \sum_{\mathbf{k}_e, \mathbf{k}_h} \tilde{\Psi}_{l_e l_h, I}(\mathbf{k}_e, \mathbf{k}_h) \hat{c}_{l_e, \mathbf{k}_e}^\dagger \hat{d}_{l_h, \mathbf{k}_h}^\dagger \quad (12)$$

is the exciton creation operator, $|0\rangle$ is the ground-state ket, and $\tilde{\Psi}_I(\mathbf{k}_e, \mathbf{k}_h)$ is the exciton wave function. By the variation method, $\delta[(\langle X_I | \hat{\mathcal{H}} | X_I \rangle - \lambda)(\langle X_I | X_I \rangle - 1)] = 0$, an eigenvalue equation can be derived as

$$\sum_{\mathbf{k}'_e, \mathbf{k}'_h} \tilde{\mathcal{H}}_X(\mathbf{k}_e, \mathbf{k}_h; \mathbf{k}'_e, \mathbf{k}'_h) \tilde{\Psi}_I(\mathbf{k}'_e, \mathbf{k}'_h) = \varepsilon_{X,I} \tilde{\Psi}_I(\mathbf{k}_e, \mathbf{k}_h), \quad (13)$$

$$\mathcal{H}_X(\mathbf{r}_e, \mathbf{r}_h) = \frac{1}{N} \sum_{\Delta \mathbf{k}_e, \Delta \mathbf{k}_h} \exp(i \Delta \mathbf{k}_e \cdot \mathbf{r}_e) \exp(i \Delta \mathbf{k}_h \cdot \mathbf{r}_h) \tilde{\mathcal{H}}_X(\mathbf{k}_e + \Delta \mathbf{k}_e, \mathbf{k}_h + \Delta \mathbf{k}_h; \mathbf{k}_e, \mathbf{k}_h), \quad (14)$$

and it is written as

$$\mathcal{H}_X(\mathbf{r}_e, \mathbf{r}_h) = \begin{pmatrix} \mathcal{H}_{11}(\mathbf{r}_e, \mathbf{r}_h) & 0 & \mathcal{T}_h(\mathbf{r}_e, \mathbf{r}_h) & \mathcal{T}_e(\mathbf{r}_e, \mathbf{r}_h) \\ 0 & \mathcal{H}_{22}(\mathbf{r}_e, \mathbf{r}_h) & \mathcal{T}_e^*(\mathbf{r}_e, \mathbf{r}_h) & \mathcal{T}_h^*(\mathbf{r}_e, \mathbf{r}_h) \\ \mathcal{T}_h^*(\mathbf{r}_e, \mathbf{r}_h) & \mathcal{T}_e(\mathbf{r}_e, \mathbf{r}_h) & \mathcal{H}_{12}(\mathbf{r}_e, \mathbf{r}_h) & 0 \\ \mathcal{T}_e^*(\mathbf{r}_e, \mathbf{r}_h) & \mathcal{T}_h(\mathbf{r}_e, \mathbf{r}_h) & 0 & \mathcal{H}_{21}(\mathbf{r}_e, \mathbf{r}_h) \end{pmatrix}, \quad (15)$$

where $\mathcal{T}_e(\mathbf{r}_e, \mathbf{r}_h) = t_e(\mathbf{r}_e)$, $\mathcal{T}_h(\mathbf{r}_e, \mathbf{r}_h) = t_h(\mathbf{r}_e)$ are interlayer charge-transfer couplings,

$$\mathcal{H}_{l_e l_h}(\mathbf{r}_e, \mathbf{r}_h) = \Delta_{l_e l_h} + \frac{|\mathbf{p}_e - \boldsymbol{\kappa}_{l_e}|^2}{2m_{e,l_e}} + \frac{|\mathbf{p}_h + \boldsymbol{\kappa}_{l_h}|^2}{2m_{h,l_h}} + U_{l_e}(\mathbf{r}_e) - U_{l_h}(\mathbf{r}_h) - W_{l_e l_h}(\mathbf{r}_{eh}), \quad (16)$$

is the layer-exciton Hamiltonian, $\Delta_{l_e l_h} = \epsilon_{e,l_e} + \epsilon_{h,l_h}$ is the band-gap energy, and $W_{l_e l_h}(\mathbf{r}) = \int e^{i\mathbf{k} \cdot \mathbf{r}} \tilde{W}(\mathbf{k}) d^2 k / (2\pi)^2$ the screened Coulomb potential. The exciton continuum model can be reformulated by the coordinate transformation from electron position and hole position coordinates to exciton COM and internal coordinates, $\mathbf{R} = \gamma_{e,l_e} \mathbf{r}_e + \gamma_{h,l_h} \mathbf{r}_h$, $\mathbf{r} = \mathbf{r}_e - \mathbf{r}_h$, with $\gamma_{e,l_e} = m_{e,l_e} / (m_{e,l_e} + m_{h,l_h})$, $\gamma_{h,l_h} = m_{h,l_h} / (m_{e,l_e} + m_{h,l_h})$, which leads to the following transformation for momentums $\mathbf{p}_e = \gamma_{e,l_e} \mathbf{P} + \mathbf{p}$, $\mathbf{p}_h = \gamma_{h,l_h} \mathbf{P} - \mathbf{p}$, with \mathbf{P} the COM momentum and \mathbf{p} the internal momentum. The same method has been used in Ref. [52]. The reciprocal basis vectors are also applied by the coordinate transformation

$$\boldsymbol{\kappa}_{l_e l_h} = \boldsymbol{\kappa}_{l_e} - \boldsymbol{\kappa}_{l_h}, \quad \boldsymbol{\kappa}_{l_e l_h} = \gamma_{h,l_h} \boldsymbol{\kappa}_{l_e} + \gamma_{e,l_e} \boldsymbol{\kappa}_{l_h}, \quad (17)$$

with $\boldsymbol{\kappa}_{l_e l_h}$ the COM reciprocal basis vector and $\boldsymbol{\kappa}_{l_e l_h}$ the internal reciprocal basis vector. The exciton Hamiltonian can be rewritten as

$$\mathcal{H}_X(\mathbf{R}, \mathbf{r}) = \begin{pmatrix} \mathcal{H}_{11}(\mathbf{R}, \mathbf{r}) & 0 & \mathcal{T}_h(\mathbf{R}, \mathbf{r}) & \mathcal{T}_e(\mathbf{R}, \mathbf{r}) \\ 0 & \mathcal{H}_{22}(\mathbf{R}, \mathbf{r}) & \mathcal{T}_e^*(\mathbf{R}, \mathbf{r}) & \mathcal{T}_h^*(\mathbf{R}, \mathbf{r}) \\ \mathcal{T}_h^*(\mathbf{R}, \mathbf{r}) & \mathcal{T}_e(\mathbf{R}, \mathbf{r}) & \mathcal{H}_{12}(\mathbf{R}, \mathbf{r}) & 0 \\ \mathcal{T}_e^*(\mathbf{R}, \mathbf{r}) & \mathcal{T}_h(\mathbf{R}, \mathbf{r}) & 0 & \mathcal{H}_{21}(\mathbf{R}, \mathbf{r}) \end{pmatrix}, \quad (18)$$

where

$$\mathcal{T}_e(\mathbf{R}, \mathbf{r}) = w_e \{ 1 + \exp[i\mathbf{g}_1 \cdot (\mathbf{R} + \gamma_{h,l_h} \mathbf{r})] + \exp[i\mathbf{g}_2 \cdot (\mathbf{R} + \gamma_{h,l_h} \mathbf{r})] \}, \quad (19)$$

$$\mathcal{T}_h(\mathbf{R}, \mathbf{r}) = w_h \{ 1 + \exp[-i\mathbf{g}_1 \cdot (\mathbf{R} - \gamma_{e,l_e} \mathbf{r})] + \exp[-i\mathbf{g}_2 \cdot (\mathbf{R} - \gamma_{e,l_e} \mathbf{r})] \}, \quad (20)$$

$$\mathcal{H}_{l_e l_h}(\mathbf{R}, \mathbf{r}) = \Delta_{l_e l_h} + \frac{|\mathbf{P} - \boldsymbol{\kappa}_{l_e l_h}|^2}{2m_{X,l_e l_h}} + \frac{|\mathbf{p} - \boldsymbol{\kappa}_{l_e l_h}|^2}{2\mu_{X,l_e l_h}} + \mathcal{V}_{l_e l_h}(\mathbf{R}, \mathbf{r}) - W_{l_e l_h}(\mathbf{r}), \quad (21)$$

with $m_{X,l_e l_h}$ the exciton mass, $\mu_{X,l_e l_h}$ the reduced mass, and $\mathcal{V}_{l_e l_h}(\mathbf{R}, \mathbf{r})$ the exciton moiré potential. The exciton mass and the reduced mass are given by

$$m_{X,l_e l_h} = m_{e,l_e} + m_{h,l_h}, \quad \mu_{X,l_e l_h} = \frac{m_{e,l_e} m_{h,l_h}}{m_{X,l_e l_h}}. \quad (22)$$

The exciton moiré potential is a combination of the electron moiré potential and the hole moiré potential. The exciton moiré potential is given by

$$\mathcal{V}_{l_e l_h}(\mathbf{R}, \mathbf{r}) = U_{l_e}(\mathbf{R} + \gamma_{h,l_h} \mathbf{r}) - U_{l_h}(\mathbf{R} - \gamma_{e,l_e} \mathbf{r}). \quad (23)$$

where $\tilde{\mathcal{H}}_X(\mathbf{k}_e, \mathbf{k}_h; \mathbf{k}'_e, \mathbf{k}'_h) = \langle 0 | \hat{a}_{l_h, \mathbf{k}_h} \hat{c}_{l_e, \mathbf{k}_e} \hat{\mathcal{H}}_{l_e, \mathbf{k}'_e} \hat{c}_{l_h, \mathbf{k}'_h}^\dagger \hat{a}_{l_e, \mathbf{k}'_e}^\dagger | 0 \rangle$ is the momentum-space exciton Hamiltonian, and $\varepsilon_{X,I}$ is the exciton eigenenergy. The continuum model to describe excitons in 2D moiré superlattices can be derived from the Fourier transform of the momentum-space exciton Hamiltonian

Note that the exciton band minimum is centered at $\boldsymbol{\kappa}_{l_e l_h} = \boldsymbol{\kappa}_{l_e} - \boldsymbol{\kappa}_{l_h}$. For intralayer excitons $l_e = l_h = l$ thus $\boldsymbol{\kappa}_{l_e l_h} = 0$, the exciton band minimum locates at the γ point in MBZ. For the interlayer exciton, $l_e = 1, l_h = 2$ or $l_e = 2, l_h = 1$ thus $\boldsymbol{\kappa}_{l_e l_h} = \pm(\boldsymbol{\kappa}_2 - \boldsymbol{\kappa}_1)$, the exciton band minimum locates at one of the κ, κ' points in the MBZ. Based on Fig. 1(b), the momentum shift of interlayer excitons comes from the momentum difference between \mathbf{K}_1 (\mathbf{K}'_1) and \mathbf{K}_2 (\mathbf{K}'_2) points on the Brillouin zones of the top and bottom layers. Therefore, the intralayer exciton is assigned as a direct exciton and the interlayer exciton is assigned as an indirect

exciton. Optical transitions only occur for intralayer excitons located at $\mathbf{K} = \mathbf{0}$, which is the γ point on the MBZ of excitons.

It is worth mentioning that, by Taylor expansion of the internal coordinate, the exciton moiré potential can be approximated as

$$\mathcal{V}_{l_e l_h}(\mathbf{R}, \mathbf{r}) \simeq U_{l_e}(\mathbf{R}) + \gamma_{h, l_h} \mathbf{r} \cdot \nabla_{\mathbf{R}} U_{l_e}(\mathbf{R}) - U_{l_h}(\mathbf{R}) + \gamma_{e, l_e} \mathbf{r} \cdot \nabla_{\mathbf{R}} U_{l_h}(\mathbf{R}). \quad (24)$$

For intralayer excitons, $l_e = l_h = l$ and $\psi_l = -(-1)^l \pi/2$ are used, and the exciton moiré potential becomes

$$\mathcal{V}_{ll}(\mathbf{R}, \mathbf{r}) \simeq 2V_l (-1)^l \sum_{j=1,3,5} (\mathbf{g}_j \cdot \mathbf{r}) \cos(\mathbf{g}_j \cdot \mathbf{R}). \quad (25)$$

On the other hand, for interlayer excitons, $l_e = 2$ and $l_h = 1$, the exciton moiré potential becomes

$$\mathcal{V}_{21}(\mathbf{R}, \mathbf{r}) \simeq 2(V_1 + V_2) \sum_{j=1,3,5} \sin(\mathbf{g}_j \cdot \mathbf{R}). \quad (26)$$

Therefore, exciton moiré potentials for intralayer excitons and interlayer excitons are different. Additionally, the exciton moiré potential jointly couples the COM motion and the internal motion. The COM wave function and the internal wave function of an intralayer moiré exciton are entangled for any moiré potential depths.

D. Exciton wave function

The exciton wave function and exciton band structure can be solved by the eigenvalue problem

$$\mathcal{H}_X(\mathbf{R}, \mathbf{r}) \Psi_{X, l\mathbf{K}}(\mathbf{R}, \mathbf{r}) = \varepsilon_{X, l\mathbf{K}} \Psi_{X, l\mathbf{K}}(\mathbf{R}, \mathbf{r}), \quad (27)$$

where $\Psi_{X, l\mathbf{K}}(\mathbf{R}, \mathbf{r})$ is the exciton wave function and $\varepsilon_{X, l\mathbf{K}}$ is the exciton eigenenergy. A variational exciton wave function method is used to solve the exciton Hamiltonian. To include the entanglement between the COM motion and the internal motion, the variational exciton wave function should contain a direct product of the COM-coordinate function and the internal-coordinate function. Such variational exciton wave function is written as

$$\Psi_{X, l\mathbf{K}}(\mathbf{R}, \mathbf{r}) = \frac{e^{i\mathbf{K} \cdot \mathbf{R}}}{2\pi} \sum_{l_e l_h, a, \mathbf{G}} C_{(l_e l_h, a, \mathbf{G}), l\mathbf{K}} \chi_{\mathbf{G}}(\mathbf{R}) \times \exp(i\kappa_{l_e l_h} \cdot \mathbf{r}) \phi_{l_e l_h, a}(\mathbf{r}) \mathbb{E}_{l_e l_h}, \quad (28)$$

where $C_{(l_e l_h, a, \mathbf{G}), l\mathbf{K}}$ is the variational wave function coefficient, $\chi_{\mathbf{G}}(\mathbf{R})$ is the COM-coordinate basis function, $\phi_{l_e l_h, a}(\mathbf{r})$ is the internal-coordinate basis function, and $\mathbb{E}_{l_e l_h}$ is the exciton Hamiltonian-matrix basis vector with

$$\mathbb{E}_{11} = \begin{pmatrix} 1 \\ 0 \\ 0 \\ 0 \end{pmatrix}, \quad \mathbb{E}_{22} = \begin{pmatrix} 0 \\ 1 \\ 0 \\ 0 \end{pmatrix}, \quad \mathbb{E}_{12} = \begin{pmatrix} 0 \\ 0 \\ 1 \\ 0 \end{pmatrix}, \quad \mathbb{E}_{21} = \begin{pmatrix} 0 \\ 0 \\ 0 \\ 1 \end{pmatrix}. \quad (29)$$

The exciton COM degree of freedom can be solved as the problem of a particle in a periodic potential. Therefore, the COM-coordinate basis function is given by the plane-wave

function

$$\chi_{\mathbf{G}}(\mathbf{R}) = e^{-i\mathbf{G} \cdot \mathbf{R}}, \quad (30)$$

where \mathbf{G} is the reciprocal-lattice vector. The exciton internal degree of freedom can be treated as the eigenspectrum problem of an isolated exciton. It is known that STOs can be used as the basis function to solve exciton internal wave functions accurately in two dimensions [53–56]. The internal-coordinate basis function is given by STOs, which have the form

$$\phi_{l_e l_h, a}(\mathbf{r}) = (e^{iL_a \varphi} / \sqrt{2\pi}) r^{N_a - 1} \exp(-Z_{l_e l_h, a} r), \quad (31)$$

with N_a the shell number, L_a the angular momentum, and $Z_{l_e l_h, a}$ the shielding constant. Note that the phase factor $\exp(i\kappa_{l_e l_h} \cdot \mathbf{r})$ has been added in Eq. (28). This phase factor is utilized to shift the internal momentum to center the origin point,

$$\exp(-i\kappa_{l_e l_h} \cdot \mathbf{r})(\mathbf{p} - \kappa_{l_e l_h}) \exp(i\kappa_{l_e l_h} \cdot \mathbf{r}) = \mathbf{p}, \quad (32)$$

such that the matrix element can be written in a simpler form. Matrix elements of the exciton Hamiltonian matrix and the overlap matrix span by the present basis are shown in Appendix B.

By using the exciton wave function, the radius and angular momentum of the hybridized moiré exciton can be found. The exciton radius operator is defined by the matrix representation

$$r_X(\mathbf{R}, \mathbf{r}) \equiv r\mathbb{I}, \quad (33)$$

with

$$\mathbb{I} = \begin{pmatrix} 1 & 0 & 0 & 0 \\ 0 & 1 & 0 & 0 \\ 0 & 0 & 1 & 0 \\ 0 & 0 & 0 & 1 \end{pmatrix} \quad (34)$$

being a four-dimensional identity matrix. The exciton radius can be solved from

$$a_{X, l} = \int \Psi_{X, l0}^*(\mathbf{R}, \mathbf{r}) r_X(\mathbf{R}, \mathbf{r}) \Psi_{X, l0}(\mathbf{R}, \mathbf{r}) d^2 R d^2 r. \quad (35)$$

The exciton angular-momentum operator is defined as $\mathcal{L}_X(\mathbf{R}, \mathbf{r}) \equiv \mathcal{L}'_X(\mathbf{R}) + \mathcal{L}''_X(\mathbf{r})$, where

$$\mathcal{L}'_X(\mathbf{R}) = [\mathbf{R} \times (\mathbf{P} - \kappa_{l_e l_h})] \mathbb{I} \quad (36)$$

and

$$\mathcal{L}''_X(\mathbf{r}) = [\mathbf{r} \times (\mathbf{p} - \kappa_{l_e l_h})] \mathbb{I} \quad (37)$$

are the matrix representations of the exciton COM angular-momentum operator and the exciton internal angular-momentum operator. Since the internal angular momentum of optically active excitons should be zero, the root-mean-square exciton angular momentum is used to measure the contribution of nonzero-angular-momentum Rydberg excitons on moiré exciton wave function. The root-mean-square exciton angular momentum $(\langle \mathcal{L}_X'^2 \rangle)^{1/2}$ is given by the formula

$$\langle \mathcal{L}_X'^2 \rangle_l = \int \Psi_{X, l0}^*(\mathbf{R}, \mathbf{r}) \mathcal{L}_X'^2(\mathbf{r}) \Psi_{X, l0}(\mathbf{R}, \mathbf{r}) d^2 R d^2 r. \quad (38)$$

Therefore, if the exciton wave function contains the STO $\phi_{l_e l_h, a}(\mathbf{r})$ with $L_a \neq 0$, a nonzero value of root-mean-square exciton angular momentum can be found.

E. Optical absorption

Based on Fermi's golden rule, the optical absorption spectrum can be given by the formula

$$\Gamma(\omega) = \frac{2\pi}{\omega} \sum_{I,\mu} |j_{0I}^\mu|^2 \delta(\omega - E_I + E_0), \quad (39)$$

where E_I is the I th state eigenenergy, $j_{II'} = \langle I | \hat{j} | I' \rangle$ is the transition amplitude, with $|I\rangle$ the I th state ket. The transition between a one-exciton excited state and the ground state is known as the one-exciton transition. By assuming the one-exciton excited states being excited states $|I\rangle = |X_{I\mathbf{K}}\rangle$, the one-exciton transition amplitudes are given by

$$j_{0,I\mathbf{K}} = \int \mathcal{J}_X(\mathbf{r}) \Psi_{X,I\mathbf{K}}(\mathbf{R}, \mathbf{r}) d^2r d^2R, \quad (40)$$

where $\mathcal{J}_X(\mathbf{r}) = (\mathcal{J}_{11}(\mathbf{r}) \ \mathcal{J}_{22}(\mathbf{r}) \ 0 \ 0)$, with $\mathcal{J}_{ll}(\mathbf{r})$ the momentum matrix element. The momentum matrix element is given by

$$\mathcal{J}_{ll}^\pm(\mathbf{r}) = e[\mathcal{J}_{ll}^x(\mathbf{r}) \pm i\mathcal{J}_{ll}^y(\mathbf{r})]/\sqrt{2} = \delta_{\tau,\pm} \delta(\mathbf{r}) e v_{F,l}, \quad (41)$$

where $v_{F,l}$ is the Fermi velocity for each layer l . Note that τ is the valley index and the matrix element is circular-polarization selected. However, this selection can be ignored since we have not included the valley degree of freedom in this model. By using the exciton wave function, the one-exciton transition amplitude is given by

$$j_{0,I\mathbf{K}}^\pm = 2\pi \sum_{l,a} \sum_{\mathbf{G}} e v_{F,l} \delta_{\mathbf{K},\mathbf{G}} C_{(ll,a,\mathbf{G}),I\mathbf{G}} \phi_{ll,a}(\mathbf{0}). \quad (42)$$

Since only the first Brillouin zone is considered in the calculation, the selection for the COM wave vector is given by $\mathbf{K} = \mathbf{0}$ for optical absorption. The ground-state energy can be assigned as $E_0 = 0$ and the excited-state energy for every one-exciton excited state is given by $E_I = \varepsilon_{X,I\mathbf{0}}$. Combining all the information, the optical absorption spectrum can be rewritten as

$$\Gamma(\omega) = \sum_{l,\tau=\pm} \frac{|j_{0,I\mathbf{0}}^\tau|^2}{\varepsilon_{X,I\mathbf{0}}} \frac{2\eta}{(\omega - \varepsilon_{X,I\mathbf{0}})^2 + \eta^2}, \quad (43)$$

where η is a line-broadening factor. Equation (43) is the working formula for us to calculate the optical absorption spectrum of moiré heterobilayers. Note that if $C_{(ll,a,\mathbf{G}),I\mathbf{G}} = \delta_{l,1} C_{(1l,a,\mathbf{G}),I\mathbf{G}}$ in Eq. (42), the formula in Eq. (43) can be reduced to the optical absorption formula for intralayer exciton transitions in the layer $l = 1$. The interlayer exciton transition is only introduced through the wave function coefficient $C_{(ll,a,\mathbf{G}),I\mathbf{G}}$ of the I th exciton state, where each exciton state is a linear combination of intralayer and interlayer exciton wave functions.

III. APPLICATIONS

In this section, the exciton continuum model is applied to the simulation of optical absorption spectra of WSe₂/WS₂ heterobilayers and MoSe₂/WS₂ heterobilayers. Twist-angle and electric-field dependencies of optical absorption spectra are calculated and discussed. Parameters for the effective-mass band and the modified Rytova-Keldysh potential of

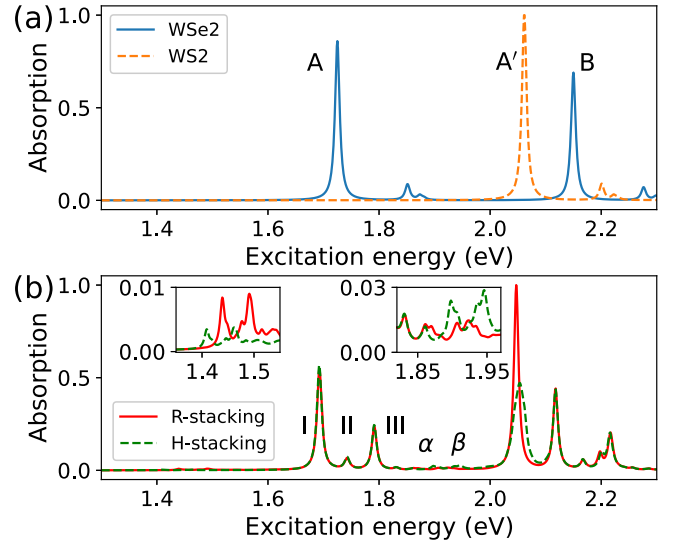


FIG. 2. (a) Calculated absorption spectra of WSe₂ and WS₂ monolayers. (b) Calculated absorption spectra of R-stacked and H-stacked WSe₂/WS₂ heterobilayers, with parameters $w_e = w_h = 20$ meV, $V_{\text{WSe}_2} = 30$ meV, $V_{\text{WS}_2} = 5$ meV, $\eta = 5$ meV, and $d = 7.0$ Å.

heterobilayers embedded in hexagonal boron nitride substrates are given in Table I. All other parameters, including moiré potential depths and charge-transfer coupling strengths, are chosen to fit simulated optical spectra with experimental observations.

A. Excitons in WSe₂/WS₂ heterobilayers

Calculated absorption spectra of WSe₂ monolayer, WS₂ monolayer, and WSe₂/WS₂ heterobilayers are shown in Figs. 2(a) and 2(b). The contributions from A and B excitons in WSe₂ monolayer and A excitons in WS₂ monolayer have been included in Fig. 2(a). Signatures of 2s, 3s Rydberg excitons in WSe₂ monolayer are also shown around 1.85 eV for A excitons and around 2.25 eV for B excitons as the satellite peaks of the dominated 1s exciton transition peak. By including moiré potentials and charge-transfer couplings in the exciton calculation for WSe₂/WS₂ heterobilayers, signatures of intralayer and interlayer moiré excitons are shown. The three prominent peaks around 1.7–1.8 eV, labeled I, II, and III peaks as in Ref. [14], can be attributed to the intralayer moiré excitons extending from A excitons of WSe₂. The inset figures in Fig. 2(b) show enlarged peaks from optical absorption by interlayer excitons. The signature around 1.4–1.5 eV in the spectrum of the R-stacked heterobilayer can be attributed to the interlayer moiré excitons with the electron locating at \mathbf{K} valley of WS₂ monolayer and the hole locating at \mathbf{K} valley of WSe₂ monolayer. The signature around 1.4–1.5 eV in the spectrum of the H-stacked heterobilayer can be attributed to the interlayer moiré excitons with the electron locating at \mathbf{K}' valley of WS₂ monolayer and the hole locating at \mathbf{K} valley of WSe₂ monolayer. The signature around 1.85–1.95 eV in the spectrum of the H-stacked heterobilayer can be attributed to the interlayer moiré excitons with the electron locating at \mathbf{K} valley of WS₂ monolayer and the hole locating at \mathbf{K}' valley

TABLE I. Effective-mass-model parameters for TMDC monolayers. The dielectric constants for the modified Rytova-Keldysh potential are given by $\kappa_1 = 4.4$ and $\kappa_0 = 2.0$. E_{gap} is the band-gap energy, E_{edge}^v is the valence band-edge energy, E_{edge}^c is the conduction band-edge energy, E_{SO}^v is the valence-band spin-orbit splitting energy, E_{SO}^c is the conduction-band spin-orbit splitting energy, a is the lattice constant of the TMDC monolayer, m_e and m_h are effective electron and hole masses, m_0 is the bare electron mass, r_0 is the screening length, E_X is the exciton binding energy for the $1s$ -orbital exciton, v_F is the Fermi velocity, and c_0 is the light speed. The exciton binding energy is calculated by variationally solving the effective mass model with Rytova-Keldysh potential as the screened Coulomb potential. The Fermi velocity is estimated by $E_{\text{gap}} = (m_e + m_h)v_F$. The effective masses and screening lengths are acquired from Ref. [57]. The lattice constants are acquired from Ref. [58]. The band-edge energies are acquired from Ref. [59]. The spin-orbit splitting energies are acquired from Ref. [60].

Materials	E_{gap} (eV)	E_{edge}^v (eV)	E_{edge}^c (eV)	E_{SO}^v (meV)	E_{SO}^c (meV)	a (Å)	m_e/m_0	m_h/m_0	r_0 (Å)	E_X (meV)	$10^3 v_F/c_0$
MoSe ₂	1.874	-5.750	-3.876	-184	20	3.288	0.70	0.70	39	232	1.62
WS ₂	2.238	-6.190	-3.952	-425	-31	3.154	0.35	0.35	34	177	2.50
WSe ₂	1.890	-5.490	-3.600	-462	-37	3.286	0.40	0.40	45	165	2.15

of WSe₂ monolayer. Interlayer-exciton transition peaks are much less obvious in comparison with intralayer-exciton transition peaks because of the large energy difference between interlayer excitons and intralayer excitons. These signatures are overall coincident with experimental observations in the literature [15,20].

In Table II, exciton transition energies, exciton binding energies, transition amplitudes, exciton radii, and exciton root-mean-square angular momentums of exciton transitions in WSe₂ monolayer and H-stacked WSe₂/WS₂ heterobilayers are shown. Excitons α , β are two interlayer-exciton transitions of H-stacked WSe₂/WS₂ heterobilayers, as indicated in Fig. 2(b). Because the internal degree of freedom is included in the exciton calculation, intralayer excitons and interlayer excitons can have different radii and angular momentum. According to the variational exciton wave function in Eq. (28), an exciton in heterobilayers can be seen as the hybridization of various Rydberg excitons in monolayers. Therefore, hybridized excitons listed in Table II show mixture properties from different Rydberg excitons in WSe₂ monolayer.

In Figs. 3(a) and 3(b), the calculated twist-angle and electric-field dependencies of optical absorption spectra in H-stacked WSe₂/WS₂ heterobilayers are shown. For the twist-angle dependence, the three intralayer-exciton peaks I, II, and III show spectral shifts with increasing twist angles.

TABLE II. Calculated properties of A excitons in WSe₂ monolayer (top three rows) and moiré excitons in H-stacked WSe₂/WS₂ heterobilayers (remaining rows). E_{exc} is the exciton transition energy, E_X is the exciton binding energy, $|j_X|^2$ is the transition amplitude, a_X is the exciton radius, and $(\langle \mathcal{L}_X'^2 \rangle)^{1/2}$ is the exciton root-mean-square angular momentum. The properties of intralayer moiré excitons are calculated without considering the interlayer tunneling.

Excitons	E_{exc} (eV)	E_X (meV)	$ j_X ^2$ (a.u.)	a_X (Å)	$\sqrt{\langle \mathcal{L}_X'^2 \rangle}$
A-1s	1.725	165	1.000	14.0	0
A-2s	1.851	39	0.107	66.8	0
A-2p	1.830	50	0	43.0	1
I	1.690	195	0.763	19.9	0.395
II	1.739	144	0.088	16.5	0.261
III	1.789	98	0.337	39.0	0.603
α	1.898	119	0.025	38.0	0.660
β	1.947	69	0.017	56.9	1.001

The peak I converges to the A-1s exciton of WSe₂ monolayer, the peak III converges to the A-2s exciton of WSe₂ monolayer, and the peak II diminishes. For the electric-field dependence, an out-of-plane electric field is included in the model by modulating the band-edge energy of WS₂ monolayer as

$$\tilde{\epsilon}_{e,\text{WS}_2} = \epsilon_{e,\text{WS}_2} - \xi_z F_z, \quad \tilde{\epsilon}_{h,\text{WS}_2} = \epsilon_{h,\text{WS}_2} - \xi_z F_z, \quad (44)$$

where ϵ_{e,WS_2} and ϵ_{h,WS_2} are band-edge energies for the conduction band and the valence band, ξ_z is the out-of-plane electric dipole moment, and F_z is the out-of-plane electric-field strength. The electric dipole moment is assigned as $\xi_z = 0.4e \text{ nm}$, where e denotes the elementary charge. Signatures of hybridization can be found in both the twist-angle dependence and the electric-field dependence, particularly near the A-exciton transition energy of the WS₂ monolayer. As shown in Fig. 3(a), signatures of avoided crossings are found at 7° twist angle and around 2.1 eV excitation energy. In Fig. 3(b), signatures of avoiding crossing are found around

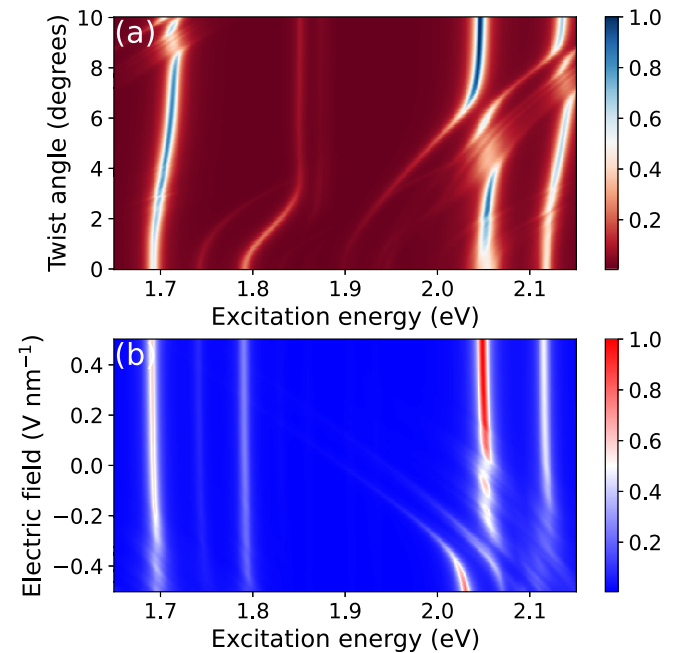


FIG. 3. (a) Calculated twist-angle dependence and (b) electric-field dependence of optical absorption spectra of H-stacked WSe₂/WS₂ heterobilayers.

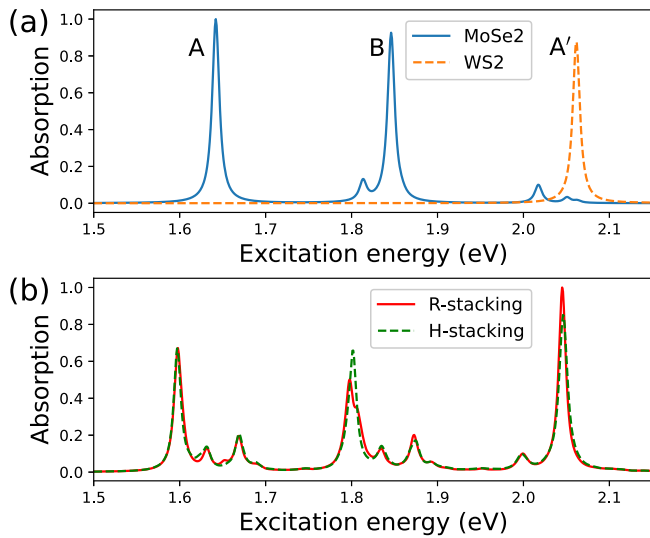


FIG. 4. (a) Calculated absorption spectra of MoSe₂ and WS₂ monolayers. (b) Calculated absorption spectra of R-stacked and H-stacked MoSe₂/WS₂ heterobilayers, with parameters $w_e = w_h = 10$ meV, $V_{\text{MoSe}_2} = 35$ meV, $V_{\text{WS}_2} = 5$ meV, $\eta = 5$ meV, and $d = 7.0$ Å.

$-0.3 - 0.5$ V nm⁻¹ electric field and around 2.1 eV excitation energy. These signatures indicate the hybridization between intralayer excitons and interlayer excitons through charge-transfer couplings as the excitation energies of intralayer excitons and interlayer excitons are close.

Note that, for real-world experiments, the moiré heterobilayer is embedded in a dielectric substrate, which is normally composed of multiple layers of hexagonal boron nitrides (hBNs) or silicon dioxide (SiO₂), and the applied external electric field can be screened by the substrate. Therefore, the out-of-plane electric field mentioned above is the out-of-plane displacement field and the simulated electric-field dependence might be different from the experimental observation due to different dielectric screening for different experimental conditions.

B. Excitons in MoSe₂/WS₂ heterobilayers

Calculated absorption spectra of MoSe₂ monolayer, WS₂ monolayer, R-stacked and H-stacked MoSe₂/WS₂ heterobilayers are shown in Figs. 4(a) and 4(b). Again, optical absorption signatures of A excitons, B excitons, and 2s, 3s Rydberg excitons of MoSe₂ monolayer and WS₂ monolayer are shown in Fig. 4(a). The interlayer-exciton transition energy of the R-stacked heterobilayer is close to the A-exciton transition energy of MoSe₂ monolayer and the interlayer-exciton transition energy of the H-stacked heterobilayer is close to the B-exciton transition energy of MoSe₂ monolayer. The hybridization between the intralayer excitons and the interlayer excitons induces small changes in the shape of peaks around the A-exciton transition energy of MoSe₂ monolayer (1.6–1.7 eV) for the R-stacked heterobilayer and around the B-exciton transition energy of MoSe₂ monolayer (1.8–1.9 eV) for the H-stacked heterobilayer.

In Fig. 5, calculated twist-angle-dependent absorption spectra of R-stacked MoSe₂/WS₂ heterobilayers and

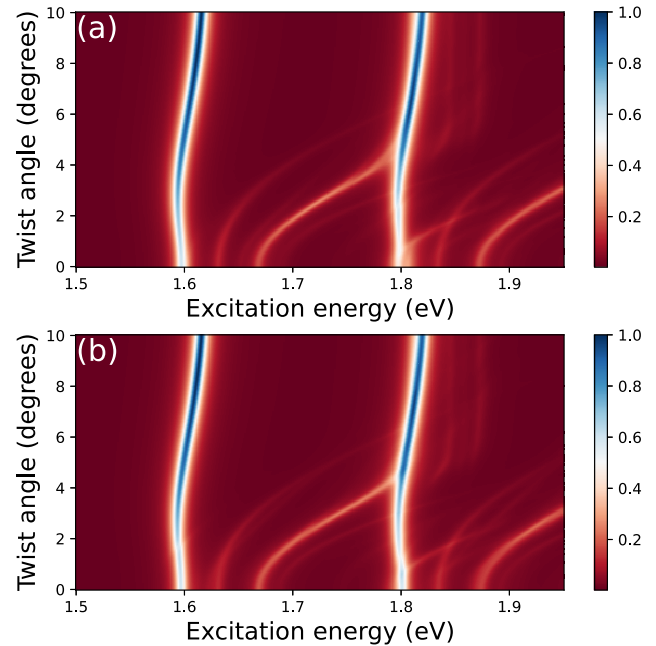


FIG. 5. Calculated twist-angle-dependent absorption spectra of (a) R-stacked MoSe₂/WS₂ heterobilayers and (b) H-stacked MoSe₂/WS₂ heterobilayers.

H-stacked MoSe₂/WS₂ heterobilayers are shown, and in Fig. 6, calculated electric-field-dependent absorption spectra of R-stacked MoSe₂/WS₂ heterobilayers and H-stacked MoSe₂/WS₂ heterobilayers are shown. The out-of-plane electric field is included in the model by the same band-edge modulation of WS₂ monolayer in Eq. (44). Signatures of avoiding crossing due to exciton hybridization can be found in

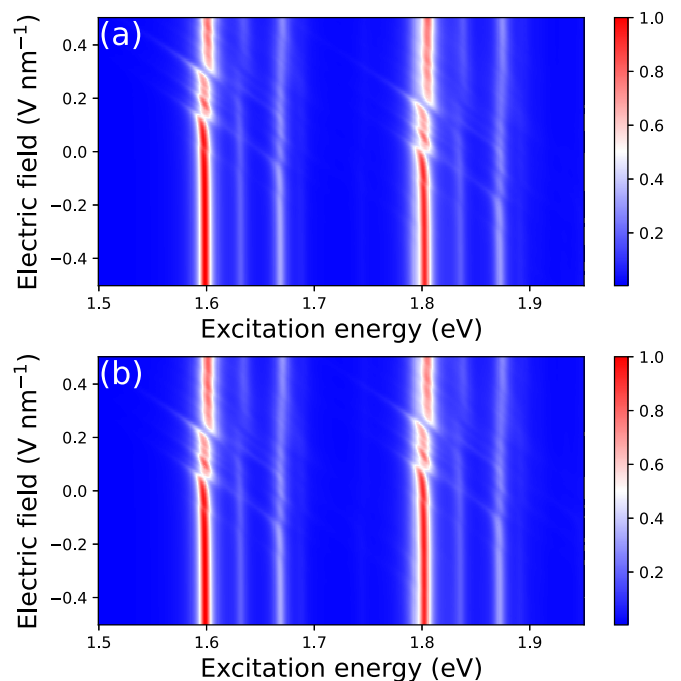


FIG. 6. Calculated electric-field-dependent absorption spectra of (a) R-stacked MoSe₂/WS₂ heterobilayers and (b) H-stacked MoSe₂/WS₂ heterobilayers.

both simulated spectra. Experimental twist-angle-dependent absorption spectra of R-stacked and H-stacked $\text{MoSe}_2/\text{WS}_2$ heterobilayers can be found in Ref. [13]. Experimental electric-field-dependent absorption spectra of R-stacked $\text{MoSe}_2/\text{WS}_2$ heterobilayers can be found in Ref. [20]. The simulation and the observation share resemblances but also noticeable differences. Those differences might be attributed to the simplicity of the present model. Particularly, intervalley exciton exchange, spin-flip interlayer charge transfer, and electron-phonon coupling are ignored. Some exciton transition signatures could be lost due to the omission. However, since it is important to test the limit of the proposed model and the context of this article is already quite ample, we will leave those topics to future works.

IV. DISCUSSIONS AND CONCLUSION

A critical issue we have not discussed is the properness of parameters chosen in the exciton continuum model. Apart from the parameters also used in monolayers, four parameters decide the optical spectra of heterobilayers: two moiré potential depths V_1 , V_2 and two charge-transfer coupling strength w_e , w_h . These parameters can be obtained by fitting observed optical spectra, as what we have done in this work, or calculated by atomistic simulation. However, there is an inconsistency between the moiré potential depths acquired from atomistic simulation and fitting the spectrum. By DFT calculation, moiré potential depths on MoSe_2 layer and WSe_2 layer of different heterobilayers are estimated to be around 8–10 meV (peak-to-peak energy difference around 80–100 meV) [43]. Via various simulations including this work by exciton continuum models, observed moiré-exciton signatures can only be explained by larger moiré potential depths about 15–35 meV [14,25]. The discrepancy may be attributed to the oversimplification of the effective moiré potential, the insufficiency of DFT calculation to simulate atom-atom potential without sufficient good van der Waals density functionals [61], or the underestimation of geometry relaxation and strain in moiré heterobilayer [25]. A theoretical work eliminates the oversimplification by using DFT calculation to simulate moiré excitons atomistically [43]. They found that one of the moiré-exciton signatures can be attributed to the charge-transfer exciton across different moiré unit cells, and the low moiré potential depth (≈ 9 meV) is sufficient to explain all intralayer moiré-exciton signatures. However, we do not reach the same conclusion since all radii of intralayer moiré excitons calculated in this work and listed in Table II are shorter than the moiré lattice constant ($a_M \approx 80$ Å) of WSe_2/WS_2 heterobilayers. A scanning tunneling microscopy experiment on twisted TMDC heterobilayers also indicates that DFT calculations might underestimate the moiré potential depths [62]. Further investigation on this issue is required in future works.

Note that the exciton continuum model in this study is only applied to the simulation of the optical spectrum of WSe_2/WS_2 and $\text{MoSe}_2/\text{WS}_2$ heterobilayers with small twist angles. This is because the present model is still too simple to accurately simulate twisted TMDC homobilayers or twisted TMDC heterobilayers with large twist angles. Several critical elements are not considered in this model. One is the valley

degree of freedom of TMDCs, which is related to the optical selection rule of circular-polarized light. Another is the mirror-symmetry-breaking interaction, which should exist in chiral or helical materials. Without these elements, the chirality and optical activity of twisted TMDC bilayers cannot be described correctly, and thus the electronic structure of twisted TMDC bilayers may not be simulated accurately by this model. Additionally, as mentioned in Sec. III B, intervalley exciton exchange and spin-flip interlayer charge transfer are ignored in this model. These effects are also related to the valley degree of freedom and this ignorance might also contribute to inaccuracy. Since this article is already lengthy, we decided to keep the simplicity of this model and omit these elements. In future works, we intend to include the valley degree of freedom and the mirror-symmetry-breaking interaction in an improved model and study a broader range of twisted TMDC bilayers.

Although this exciton continuum model might suffer from oversimplification, it can be beneficial with its simplicity for future extended studies. For example, in this work, only lattice mismatch and twist angle on the moiré pattern are considered, and the rotational symmetry of the system is not broken. However, in reality, the threefold rotational symmetry of moiré heterobilayers could be broken in the presence of the uniaxial strain, and the optical properties of interlayer and hybrid excitons would be affected by the symmetry breaking. The modification could be done by including a pseudogauge potential in terms of strain tensor components [63,64]. Another example is that exciton complexes such as trions and biexcitons are known to be computationally exhausting to simulate. It is easier to use effective-mass models and variational wave functions to study exciton complexes [55,56]. It is a natural extension of our theory to build the theoretical framework of using continuum models and variational wave functions to study hybridized moiré exciton complexes in multilayer materials. Additionally, with the future inclusion of intervalley exchange and electron-phonon coupling into this model, charge and exciton dynamics in moiré materials could also be studied without excessively exhausting computation.

In conclusion, we propose a continuum model to study hybridized moiré excitons in TMDC heterobilayers. A variational wave function method is used to solve this model. We use the present theory to study optical absorption spectra of WSe_2/WS_2 and $\text{MoSe}_2/\text{WS}_2$ heterobilayers. A good correspondence between theoretical simulation and experimental observation of moiré excitons is found. This model could set the foundation of a theoretical framework to study the physical properties of moiré excitons in different moiré materials.

ACKNOWLEDGMENTS

This work was supported by the National Science and Technology Council of Taiwan, the Ministry of Education (Higher Education Sprout Project No. NTU-112L104022), and the National Center for Theoretical Sciences of Taiwan.

APPENDIX A: MODIFIED RYTOVA-KELDYSH POTENTIAL

The modified Rytova-Keldysh potential for parallel bilayers is derived in this section. The notation and formulation of

the present derivation are taken from Ref. [65].

1. Reduced Green's function

The Poisson equation for electrostatics in three-dimensional (3D) free space is written as

$$\nabla^2 \Phi(\mathbf{r}) = -\rho(\mathbf{r})/\kappa, \quad (\text{A1})$$

where $\Phi(\mathbf{r})$ is the electrostatic potential, $\rho(\mathbf{r})$ is the charge density, and κ is the dielectric constant. The charge-free electrostatic potential can be solved by the Laplace equation, $\nabla^2 \Phi(\mathbf{r}) = 0$. The formal solution of the Poisson equation in three-dimensional free space is given by

$$\Phi(\mathbf{r}) = \frac{1}{\kappa} \int \frac{\rho(\mathbf{r}')}{|\mathbf{r} - \mathbf{r}'|} d^3r'. \quad (\text{A2})$$

The Green's function at a point \mathbf{r} interacting with the point charge e at \mathbf{r}' in 3D space is given by

$$G(\mathbf{r}, \mathbf{r}') = \frac{1}{\kappa |\mathbf{r} - \mathbf{r}'|}. \quad (\text{A3})$$

Since $\nabla^2(1/r) = -4\pi\delta(\mathbf{r})$ and thus

$$\kappa \nabla^2 G(\mathbf{r}, \mathbf{r}') = -4\pi\delta(\mathbf{r} - \mathbf{r}'), \quad (\text{A4})$$

Green's function is a solution of the Poisson equation. The Green's function can also be derived from solving Eq. (A4). By using the property of the δ function,

$$\delta(\mathbf{r} - \mathbf{r}') = \int \frac{d^3k}{(2\pi)^3} e^{i\mathbf{k}\cdot(\mathbf{r}-\mathbf{r}')}, \quad (\text{A5})$$

and the derivative $\nabla e^{i\mathbf{k}\cdot(\mathbf{r}-\mathbf{r}')} = i\mathbf{k}e^{i\mathbf{k}\cdot(\mathbf{r}-\mathbf{r}')}$, the Fourier transform of Green's function can be found as

$$G(\mathbf{r}, \mathbf{r}') = \int \frac{d^3k}{(2\pi)^3} \frac{4\pi}{\kappa k^2} e^{i\mathbf{k}\cdot(\mathbf{r}-\mathbf{r}')}. \quad (\text{A6})$$

Singling out the z direction in a 3D free space, Eq. (A6) can be rewritten as

$$G(\mathbf{r}, \mathbf{r}') = \frac{4\pi}{\kappa} \int \frac{dk_x dk_y}{(2\pi)^2} e^{i[k_x(x-x') + k_y(y-y')]} \times \int \frac{dk_z}{2\pi} \frac{e^{ik_z(z-z')}}{k_x^2 + k_y^2 + k_z^2}. \quad (\text{A7})$$

By using

$$\int_{-\infty}^{\infty} \frac{dk_z}{2\pi} \frac{e^{ik_z(z-z')}}{k_x^2 + k_y^2 + k_z^2} = \frac{1}{2k_{\parallel}} e^{-k_{\parallel}|z-z'|}, \quad (\text{A8})$$

with $k_{\parallel}^2 = k_x^2 + k_y^2$, the Green's function becomes

$$G(\mathbf{r}, \mathbf{r}') = 4\pi \int \frac{d^2k_{\parallel}}{(2\pi)^2} e^{i\mathbf{k}_{\parallel}\cdot(\mathbf{r}_{\parallel}-\mathbf{r}'_{\parallel})} g(z, z'; k_{\parallel}), \quad (\text{A9})$$

where $\mathbf{r}_{\parallel} = (x, y)$ is the 2D coordinates, $\mathbf{k}_{\parallel} = (k_x, k_y)$ is the 2D k vector, and

$$g(z, z'; k_{\parallel}) = \frac{1}{2\kappa k_{\parallel}} e^{-k_{\parallel}|z-z'|} \quad (\text{A10})$$

is the reduced Green's function. The differential equation for the reduced Green's function can be found as

$$\kappa \left[k_{\parallel}^2 - \frac{\partial^2}{\partial z^2} \right] g(z, z'; k_{\parallel}) = \delta(z - z'). \quad (\text{A11})$$

By these two integrals over the infinitesimal segment near $z = z'$,

$$\int_{z'-0}^{z'+0} dz \left[k_{\parallel}^2 - \frac{\partial^2}{\partial z^2} \right] g(z, z'; k_{\parallel}) = \int_{z'-0}^{z'+0} dz \frac{\delta(z - z')}{\kappa}, \quad (\text{A12})$$

$$\int_{z'-0}^{z'+0} dz \left[k_{\parallel}^2 - \frac{\partial^2}{\partial z^2} \right] g(z, z'; k_{\parallel}) = \int_{z'-0}^{z'+0} dz \frac{\delta(z - z')}{\kappa}. \quad (\text{A13})$$

The first equation gives

$$-\frac{\partial g}{\partial z} \Big|_{z=z'+0} + \frac{\partial g}{\partial z} \Big|_{z=z'-0} = \frac{1}{\kappa}, \quad (\text{A14})$$

with 0 indicating an infinitesimal value, and the second equation becomes

$$-\int_{z'-0}^{z'+0} dz \frac{\partial^2}{\partial z^2} g(z, z'; k_{\parallel}) = \frac{z'}{\kappa}, \quad (\text{A15})$$

and then becomes

$$-z \frac{\partial g}{\partial z} \Big|_{z'-0}^{z'+0} + \int_{z'-0}^{z'+0} dz \frac{\partial g}{\partial z} = \frac{z'}{\kappa}. \quad (\text{A16})$$

By using Eq. (A14), it is found that

$$g|_{z=z'+0} = g|_{z=z'-0}. \quad (\text{A17})$$

The equation indicates the continuity condition for the solution of the Poisson equation. Equations (A14) and (A17) indicate that the g is continuous and $\partial g/\partial z$ is discontinuous at $z = z'$.

2. Rytova-Keldysh potential in parallel bilayers

The parallel bilayers separate three regimes. Two are uniform dielectric materials $z < 0$, $z > d$. The regime in the middle $0 < z < d$ is an empty space. The Green's function is written as

$$z \leq 0 : \kappa_1 \nabla^2 G(\mathbf{r}, \mathbf{r}') = -4\pi[\delta(\mathbf{r} - \mathbf{r}') + \sigma_1 \delta(z)], \quad (\text{A18})$$

$$0 < z < d : \kappa_0 \nabla^2 G(\mathbf{r}, \mathbf{r}') = -4\pi\delta(\mathbf{r} - \mathbf{r}'), \quad (\text{A19})$$

$$z \geq d : \kappa_2 \nabla^2 G(\mathbf{r}, \mathbf{r}') = -4\pi[\delta(\mathbf{r} - \mathbf{r}') + \sigma_2 \delta(z - d)], \quad (\text{A20})$$

where σ_1, σ_2 are the surface bound charges on the layers, κ_1, κ_2 are the dielectric constants of the uniform dielectric materials, and κ_0 is the dielectric constant for the empty space. The surface-bound charge can be related to the polarization of the layer by

$$\nabla_{\parallel} \cdot \mathbf{P}_{\parallel} = -\sigma, \quad (\text{A21})$$

where $\nabla_{\parallel} = (\partial/\partial x, \partial/\partial y)$ and $\mathbf{P}_{\parallel} = (P_x, P_y)$ are the divergence and the polarization on the 2D space. The polarization

can be related to the electric field by

$$\mathbf{P}_{\parallel} = \chi_{2D} \mathbf{E}_{\parallel}, \quad (\text{A22})$$

with $\mathbf{E}_{\parallel} = (E_x, E_y)$ the electric field in the two-dimensional space and χ_{2D} is the electric susceptibility (or polarizability) of the layer. Since $\mathbf{E}_{\parallel} = -\nabla_{\parallel} \Phi$, we can derive the 2D Poisson equation,

$$\chi_1 \nabla_{\parallel}^2 \Phi(\mathbf{r})|_{z=0} = \sigma_1, \quad \chi_2 \nabla_{\parallel}^2 \Phi(\mathbf{r})|_{z=d} = \sigma_2, \quad (\text{A23})$$

where χ_1 and χ_2 are the electric susceptibilities of the corresponding layers, the Green's function can be rewritten as

$$z \leq 0: \quad \kappa_1 \left[\nabla^2 + \frac{4\pi}{\kappa_1} \chi_1 \delta(z) \nabla_{\parallel}^2 \right] G(\mathbf{r}, \mathbf{r}') = -4\pi \delta(\mathbf{r} - \mathbf{r}'), \quad (\text{A24})$$

$$0 < z < d: \quad \kappa_0 \nabla^2 G(\mathbf{r}, \mathbf{r}') = -4\pi \delta(\mathbf{r} - \mathbf{r}'), \quad (\text{A25})$$

$$z \geq d: \quad \kappa_2 \left[\nabla^2 + \frac{4\pi}{\kappa_2} \chi_2 \delta(z-d) \nabla_{\parallel}^2 \right] G(\mathbf{r}, \mathbf{r}') = -4\pi \delta(\mathbf{r} - \mathbf{r}'). \quad (\text{A26})$$

By using Eq. (A9), the Poisson equation for the reduced Green's function can be written as

$$z \leq 0: \quad \kappa_1 \left[k_{\parallel}^2 - \frac{\partial^2}{\partial z^2} + \frac{4\pi \chi_1}{\kappa_1} k_{\parallel}^2 \delta(z) \right] g = \delta(z - z'), \quad (\text{A27})$$

$$0 < z < d: \quad \kappa_0 \left[k_{\parallel}^2 - \frac{\partial^2}{\partial z^2} \right] g = \delta(z - z'), \quad (\text{A28})$$

$$z \geq d: \quad \kappa_2 \left[k_{\parallel}^2 - \frac{\partial^2}{\partial z^2} + \frac{4\pi \chi_2}{\kappa_2} k_{\parallel}^2 \delta(z-d) \right] g = \delta(z - z'). \quad (\text{A29})$$

Assuming that the test charge is at $z' = 0$, the boundary conditions can be derived

$$-\kappa_0 \frac{\partial}{\partial z} g \Big|_{z=+0} + \kappa_1 \frac{\partial}{\partial z} g \Big|_{z=-0} = 1 - 4\pi \chi_1 k_{\parallel}^2 g|_{z=0}, \quad (\text{A30})$$

$$-\kappa_2 \frac{\partial}{\partial z} g \Big|_{z=d+0} + \kappa_0 \frac{\partial}{\partial z} g \Big|_{z=d-0} = -4\pi \chi_2 k_{\parallel}^2 g|_{z=d}. \quad (\text{A31})$$

The general solution of Green's function is assumed as

$$z \leq 0: \quad g = A e^{k_{\parallel} z}, \quad (\text{A32})$$

$$0 < z < d: \quad g = B e^{k_{\parallel} z} + C e^{-k_{\parallel} z}, \quad (\text{A33})$$

$$z \geq d: \quad g = D e^{-k_{\parallel} z}. \quad (\text{A34})$$

By using the continuity condition in Eq. (A17) and the boundary conditions, the four coefficients can be connected to four coupled linear equations,

$$A = B + C, \quad B e^{k_{\parallel} d} + C e^{-k_{\parallel} d} = D e^{-k_{\parallel} d}. \quad (\text{A35})$$

$$(\kappa_1 k_{\parallel} + 2\xi_1 k_{\parallel}^2) A - \kappa_0 k_{\parallel} B + \kappa_0 k_{\parallel} C = 1, \quad (\text{A36})$$

$$\kappa_0 k_{\parallel} (B e^{k_{\parallel} d} - C e^{-k_{\parallel} d}) + (\kappa_2 k_{\parallel} + 4\pi \chi_2 k_{\parallel}^2) D e^{-k_{\parallel} d} = 0. \quad (\text{A37})$$

By using the first equation $A = B + C$ in other linear equations to replace the coefficient A , we can reduce one of the four variables. We get the three coupled equations,

$$B e^{k_{\parallel} d} + C e^{-k_{\parallel} d} - D e^{-k_{\parallel} d} = 0. \quad (\text{A38})$$

$$(\lambda_1 - \kappa_0) B + (\lambda_1 + \kappa_0) C = 1/k_{\parallel}, \quad (\text{A39})$$

$$\kappa_0 B e^{k_{\parallel} d} - \kappa_0 C e^{-k_{\parallel} d} + \lambda_2 D e^{-k_{\parallel} d} = 0. \quad (\text{A40})$$

with $\lambda_1 = \kappa_1 + 4\pi\chi_1 k_{\parallel}$ and $\lambda_2 = \kappa_2 + 4\pi\chi_2 k_{\parallel}$. These equations can be rewritten as the matrix form,

$$\begin{bmatrix} \lambda_1 - \kappa_0 & \lambda_1 + \kappa_0 & 0 \\ e^{k_{\parallel}d} & e^{-k_{\parallel}d} & -e^{-k_{\parallel}d} \\ \kappa_0 e^{k_{\parallel}d} & -\kappa_0 e^{-k_{\parallel}d} & \lambda_2 e^{-k_{\parallel}d} \end{bmatrix} \begin{bmatrix} B \\ C \\ D \end{bmatrix} = \begin{bmatrix} 1/k_{\parallel} \\ 0 \\ 0 \end{bmatrix}. \quad (\text{A41})$$

By Cramer's rule, these coefficients can be solved as

$$B = \frac{1}{\text{Det}} \begin{vmatrix} 1/k_{\parallel} & \lambda_1 + \kappa_0 & 0 \\ 0 & e^{-k_{\parallel}d} & -e^{-k_{\parallel}d} \\ 0 & -\kappa_0 e^{-k_{\parallel}d} & \lambda_2 e^{-k_{\parallel}d} \end{vmatrix} = \frac{(\lambda_2 - \kappa_0)e^{-2k_{\parallel}d}}{k_{\parallel}\text{Det}}, \quad (\text{A42})$$

$$C = \frac{1}{\text{Det}} \begin{vmatrix} \lambda_1 - \kappa_0 & 1/k_{\parallel} & 0 \\ e^{k_{\parallel}d} & 0 & -e^{-k_{\parallel}d} \\ \kappa_0 e^{k_{\parallel}d} & 0 & \lambda_2 e^{-k_{\parallel}d} \end{vmatrix} = -\frac{\lambda_2 + \kappa_0}{k_{\parallel}\text{Det}}, \quad (\text{A43})$$

$$D = \frac{1}{\text{Det}} \begin{vmatrix} \lambda_1 - \kappa_0 & \lambda_1 + \kappa_0 & 1/k_{\parallel} \\ e^{k_{\parallel}d} & e^{-k_{\parallel}d} & 0 \\ \kappa_0 e^{k_{\parallel}d} & -\kappa_0 e^{-k_{\parallel}d} & 0 \end{vmatrix} = -\frac{2\kappa_0}{k_{\parallel}\text{Det}}, \quad (\text{A44})$$

$$\text{Det} = \begin{vmatrix} \lambda_1 - \kappa_0 & \lambda_1 + \kappa_0 & 0 \\ e^{k_{\parallel}d} & e^{-k_{\parallel}d} & -e^{-k_{\parallel}d} \\ \kappa_0 e^{k_{\parallel}d} & -\kappa_0 e^{-k_{\parallel}d} & \lambda_2 e^{-k_{\parallel}d} \end{vmatrix} = (\lambda_1 - \kappa_0)(\lambda_2 - \kappa_0)e^{-2k_{\parallel}d} - (\lambda_1 + \kappa_0)(\lambda_2 + \kappa_0). \quad (\text{A45})$$

Therefore, the intralayer and interlayer Rytova-Keldysh potentials can be found as

$$W_{11}(k_{\parallel}) = 4\pi g \Big|_{z=0, z'=0} = \frac{(4\pi/k_{\parallel})[(\lambda_2 + \kappa_0)e^{k_{\parallel}d} - (\lambda_2 - \kappa_0)e^{-k_{\parallel}d}]}{(\lambda_1 + \kappa_0)(\lambda_2 + \kappa_0)e^{k_{\parallel}d} - (\lambda_1 - \kappa_0)(\lambda_2 - \kappa_0)e^{-k_{\parallel}d}}, \quad (\text{A46})$$

$$W_{21}(k_{\parallel}) = 4\pi g \Big|_{z=d, z'=0} = \frac{8\pi\kappa_0/k_{\parallel}}{(\lambda_1 + \kappa_0)(\lambda_2 + \kappa_0)e^{k_{\parallel}d} - (\lambda_1 - \kappa_0)(\lambda_2 - \kappa_0)e^{-k_{\parallel}d}}. \quad (\text{A47})$$

By replacing $q = k_{\parallel}$ and using dielectric functions, these potentials can be rewritten as

$$W_{11}(q) = \frac{2\pi}{\epsilon_{11}(q)q}, \quad W_{21}(q) = \frac{2\pi}{\epsilon_{21}(q)q}, \quad (\text{A48})$$

where the intralayer and interlayer dielectric functions are written as

$$\epsilon_{11}(q) = \frac{\kappa_0\epsilon_{21}(q)}{\left(\frac{\kappa_2 + \kappa_0}{2} + r_2q\right)e^{qd} - \left(\frac{\kappa_2 - \kappa_0}{2} + r_2q\right)e^{-qd}}, \quad (\text{A49})$$

$$\epsilon_{21}(q) = \left(\frac{\kappa_1 + \kappa_0}{2} + r_1q\right)\left(\frac{\kappa_2 + \kappa_0}{2} + r_2q\right)\frac{e^{qd}}{\kappa_0} - \left(\frac{\kappa_1 - \kappa_0}{2} + r_1q\right)\left(\frac{\kappa_2 - \kappa_0}{2} + r_2q\right)\frac{e^{-qd}}{\kappa_0}, \quad (\text{A50})$$

with $r_1 = 2\pi\chi_1$ and $r_2 = 2\pi\chi_2$ being the screening lengths. By assigning $\kappa_1 = \kappa_2$, the modified Rytova-Keldysh potentials in Eqs. (9)–(11) can be derived.

APPENDIX B: MATRIX ELEMENTS OF EXCITON HAMILTONIAN

The matrix elements of the exciton Hamiltonian matrix and overlap matrix expanded by the basis functions in Sec. II D are derived. By using the variational method, the exciton wave function can be solved from the matrix eigenvalue equation:

$$\sum_{l'_c, l'_h, b} \tilde{\mathcal{H}}_{(l_c, l_h, a, \mathbf{G})(l'_c, l'_h, b, \mathbf{G}')} \cdot \mathbf{K} C_{(l'_c, l'_h, b, \mathbf{G}'), \mathbf{I} \mathbf{K}} = \epsilon_{\mathbf{X}, \mathbf{I} \mathbf{K}} \sum_b \mathcal{O}_{(l_c, l_h, a, \mathbf{G})(l_c, l_h, b, \mathbf{G}')} C_{(l_c, l_h, b, \mathbf{G}'), \mathbf{I} \mathbf{K}}. \quad (\text{B1})$$

The exciton Hamiltonian matrix elements are given by

$$\begin{aligned} \tilde{\mathcal{H}}_{(l_c, l_h, a, \mathbf{G})(l'_c, l'_h, b, \mathbf{G}')} \cdot \mathbf{K} &= \delta_{l_c, l'_c} \delta_{l_h, l'_h} \int \psi_{\mathbf{G}}^*(\mathbf{R}) \phi_{l_c, l_h, a}^*(\mathbf{r}) \tilde{\mathcal{H}}_{l_c, l_h}(\mathbf{R}, \mathbf{r}) \psi_{\mathbf{G}'}(\mathbf{R}) \phi_{l_c, l_h, b}(\mathbf{r}) d^2 R d^2 r \\ &+ (1 - \delta_{l_c, l'_c}) \delta_{l_h, l'_h} \int \psi_{\mathbf{G}}^*(\mathbf{R}) \phi_{l_c, l_h, a}^*(\mathbf{r}) \tilde{\mathcal{T}}_{e, (l_c, l_h)(l'_c, l'_h)}(\mathbf{R}, \mathbf{r}) \psi_{\mathbf{G}'}(\mathbf{R}) \phi_{l_c, l_h, b}(\mathbf{r}) d^2 R d^2 r \\ &+ \delta_{l_c, l'_c} (1 - \delta_{l_h, l'_h}) \int \psi_{\mathbf{G}}^*(\mathbf{R}) \phi_{l_c, l_h, a}^*(\mathbf{r}) \tilde{\mathcal{T}}_{h, (l_c, l_h)(l'_c, l'_h)}(\mathbf{R}, \mathbf{r}) \psi_{\mathbf{G}'}(\mathbf{R}) \phi_{l_c, l'_h, b}(\mathbf{r}) d^2 R d^2 r, \end{aligned} \quad (\text{B2})$$

with

$$\tilde{\mathcal{H}}_{l_e l_h}(\mathbf{R}, \mathbf{r}) = e^{-i\mathbf{K}\cdot\mathbf{R}} \exp(-i\boldsymbol{\kappa}_{l_e l_h} \cdot \mathbf{r}) \mathcal{H}_{l_e l_h}(\mathbf{R}, \mathbf{r}) \exp(i\boldsymbol{\kappa}_{l_e l_h} \cdot \mathbf{r}) e^{i\mathbf{K}\cdot\mathbf{R}}, \quad (\text{B3})$$

$$\tilde{\mathcal{T}}_{e,(1_h)(2_h)}(\mathbf{R}, \mathbf{r}) = e^{-i\mathbf{K}\cdot\mathbf{R}} \exp(-i\boldsymbol{\kappa}_{1_h} \cdot \mathbf{r}) \mathcal{T}_e(\mathbf{R}, \mathbf{r}) \exp(i\boldsymbol{\kappa}_{2_h} \cdot \mathbf{r}) e^{i\mathbf{K}\cdot\mathbf{R}}, \quad (\text{B4})$$

$$\tilde{\mathcal{T}}_{e,(2_h)(1_h)}(\mathbf{R}, \mathbf{r}) = e^{-i\mathbf{K}\cdot\mathbf{R}} \exp(-i\boldsymbol{\kappa}_{2_h} \cdot \mathbf{r}) \mathcal{T}_e^*(\mathbf{R}, \mathbf{r}) \exp(i\boldsymbol{\kappa}_{1_h} \cdot \mathbf{r}) e^{i\mathbf{K}\cdot\mathbf{R}}, \quad (\text{B5})$$

$$\tilde{\mathcal{T}}_{h,(l_e)(l_e)}(\mathbf{R}, \mathbf{r}) = e^{-i\mathbf{K}\cdot\mathbf{R}} \exp(-i\boldsymbol{\kappa}_{l_e} \cdot \mathbf{r}) \mathcal{T}_h(\mathbf{R}, \mathbf{r}) \exp(i\boldsymbol{\kappa}_{l_e} \cdot \mathbf{r}) e^{i\mathbf{K}\cdot\mathbf{R}}, \quad (\text{B6})$$

$$\tilde{\mathcal{T}}_{h,(l_e)(l_e)}(\mathbf{R}, \mathbf{r}) = e^{-i\mathbf{K}\cdot\mathbf{R}} \exp(-i\boldsymbol{\kappa}_{l_e} \cdot \mathbf{r}) \mathcal{T}_h^*(\mathbf{R}, \mathbf{r}) \exp(i\boldsymbol{\kappa}_{l_e} \cdot \mathbf{r}) e^{i\mathbf{K}\cdot\mathbf{R}}. \quad (\text{B7})$$

The overlap matrix elements are given by

$$\bar{O}_{(l_e l_h, a, \mathbf{G})(l_e l_h, b, \mathbf{G}')} = \int \psi_{\mathbf{G}}^*(\mathbf{R}) \phi_{l_e l_h, a}^*(\mathbf{r}) \psi_{\mathbf{G}'}(\mathbf{R}) \phi_{l_e l_h, b}(\mathbf{r}) d^2 R d^2 r. \quad (\text{B8})$$

The diagonal Hamiltonian matrix elements are given by

$$\tilde{\mathcal{H}}_{(l_e l_h, a, \mathbf{G})(l_e l_h, b, \mathbf{G}'), \mathbf{K}} = \delta_{\mathbf{G}, \mathbf{G}'} o_{ab} \left[\Delta_{l_e l_h} + \frac{|\mathbf{K} - \mathbf{G} - \boldsymbol{\kappa}_{l_e l_h}|^2}{2m_{X, l_e l_h}} \right] + \delta_{\mathbf{G}, \mathbf{G}'} \langle a | \left[-\frac{\nabla^2}{2\mu_{X, l_e l_h}} - W_{l_e l_h}(r) \right] | b \rangle + \langle a, \mathbf{G} | \mathcal{V}_{l_e l_h}(\mathbf{R}, \mathbf{r}) | b, \mathbf{G}' \rangle, \quad (\text{B9})$$

$$-\frac{1}{2\mu_{X, l_e l_h}} \langle a | \nabla^2 | b \rangle = -\frac{1}{2\mu_{X, l_e l_h}} \frac{(N_a + N_b - 1)!}{(\mathcal{Z}_{l_e l_h, a} + \mathcal{Z}_{l_e l_h, b})^{N_a + N_b}} \left\{ (1 - \delta_{N_b, 1}) \frac{[(N_b - 1)^2 - L_b^2] (\mathcal{Z}_{l_e l_h, a} + \mathcal{Z}_{l_e l_h, b})^2}{(N_a + N_b - 1)(N_a + N_b - 2)} \right. \\ \left. - \frac{[(2N_b - 1)\mathcal{Z}_{l_e l_h, b}] (\mathcal{Z}_{l_e l_h, a} + \mathcal{Z}_{l_e l_h, b})}{(N_a + N_b - 1)} + \mathcal{Z}_{l_e l_h, b}^2 \right\}, \quad (\text{B10})$$

$$\langle a | W_{l_e l_h}(\mathbf{r}) | b \rangle = \frac{\delta_{L_a, L_b}}{(2\pi)^2} \int_0^\infty \tilde{\mathcal{R}}_{N_a + N_b - 1, 0}(\mathcal{Z}_{l_e l_h, a} + \mathcal{Z}_{l_e l_h, b}, k) \tilde{W}_{l_e l_h}(k) k dk, \quad (\text{B11})$$

$$\langle a, \mathbf{G} | \mathcal{V}_{l_e l_h}(\mathbf{R}, \mathbf{r}) | b, \mathbf{G}' \rangle = \sum_{j=1,3,5} \{ V_c \exp[i(-1)^{l_e} \psi] \delta(\mathbf{G} - \mathbf{G}' + \mathbf{g}_j) \tilde{\rho}_{(l_e l_h, a)(l_e l_h, b)}(-\gamma_{h, l_h} \mathbf{g}_j) \\ + V_c \exp[-i(-1)^{l_e} \psi] \delta(\mathbf{G} - \mathbf{G}' - \mathbf{g}_j) \tilde{\rho}_{(l_e l_h, a)(l_e l_h, b)}(\gamma_{h, l_h} \mathbf{g}_j) \\ - V_h \exp[i(-1)^{l_h} \psi] \delta(\mathbf{G} - \mathbf{G}' + \mathbf{g}_j) \tilde{\rho}_{(l_e l_h, a)(l_e l_h, b)}(\gamma_{e, l_e} \mathbf{g}_j) \\ - V_h \exp[-i(-1)^{l_h} \psi] \delta(\mathbf{G} - \mathbf{G}' - \mathbf{g}_j) \tilde{\rho}_{(l_e l_h, a)(l_e l_h, b)}(-\gamma_{e, l_e} \mathbf{g}_j) \}, \quad (\text{B12})$$

with

$$\tilde{\rho}_{(l_e l_h, a)(l_e l_h, b)}(\mathbf{k}) = \frac{e^{-i(L_a - L_b)\varphi_{\mathbf{k}}}}{2\pi} \tilde{\mathcal{R}}_{N_a + N_b - 1, L_b - L_a}(\mathcal{Z}_{l_e l_h, a} + \mathcal{Z}_{l_e l_h, b}, k), \quad (\text{B13})$$

where the radial function in momentum space can be obtained by the generating formula

$$\tilde{\mathcal{R}}_{N, L}(\mathcal{Z}, k) = \frac{2\pi(-i)^N}{k^{N+1}} \frac{d^N}{dz^N} \left. \frac{[z - i(L/|L|)\sqrt{1-z^2}]^{|L|}}{\sqrt{1-z^2}} \right|_{z=i\mathcal{Z}/k}. \quad (\text{B14})$$

The nondiagonal Hamiltonian matrix elements can be rewritten as

$$\tilde{\mathcal{H}}_{(l_e l_h, a, \mathbf{G})(l_e l_h, b, \mathbf{G}'), \mathbf{K}} = w_e \delta_{l_h, l_h'} (1 - \delta_{l_e, l_e'}) \{ \delta(\mathbf{G} - \mathbf{G}') \tilde{\rho}_{(l_e l_h, a)(l_e l_h, b)} [(l_e - l_e')(\gamma_{h, l_h} \boldsymbol{\kappa}_3 + \Delta_e \boldsymbol{\kappa}_{l_h})] \\ + \delta(\mathbf{G} - \mathbf{G}' - (l_e - l_e') \mathbf{g}_1) \tilde{\rho}_{(l_e l_h, a)(l_e l_h, b)} [(l_e - l_e')(\gamma_{h, l_h} \boldsymbol{\kappa}_1 + \Delta_e \boldsymbol{\kappa}_{l_h})] \\ + \delta(\mathbf{G} - \mathbf{G}' - (l_e - l_e') \mathbf{g}_2) \tilde{\rho}_{(l_e l_h, a)(l_e l_h, b)} [(l_e - l_e')(\gamma_{h, l_h} \boldsymbol{\kappa}_5 + \Delta_e \boldsymbol{\kappa}_{l_h})] \} \\ + w_h \delta_{l_e, l_e'} (1 - \delta_{l_h, l_h'}) \{ \delta(\mathbf{G} - \mathbf{G}') \tilde{\rho}_{(l_e l_h, a)(l_e l_h, b)} [(l_h - l_h')(\gamma_{e, l_e} \boldsymbol{\kappa}_3 + \Delta_h \boldsymbol{\kappa}_{l_e})] \\ + \delta(\mathbf{G} - \mathbf{G}' + (l_h - l_h') \mathbf{g}_1) \tilde{\rho}_{(l_e l_h, a)(l_e l_h, b)} [(l_h - l_h')(\gamma_{e, l_e} \boldsymbol{\kappa}_1 + \Delta_h \boldsymbol{\kappa}_{l_e})] \\ + \delta(\mathbf{G} - \mathbf{G}' + (l_h - l_h') \mathbf{g}_2) \tilde{\rho}_{(l_e l_h, a)(l_e l_h, b)} [(l_h - l_h')(\gamma_{e, l_e} \boldsymbol{\kappa}_5 + \Delta_h \boldsymbol{\kappa}_{l_e})] \}, \quad (\text{B15})$$

with $\Delta_e = \gamma_{e,2} - \gamma_{e,1}$, $\Delta_h = \gamma_{h,2} - \gamma_{h,1}$. The overlap matrix element is given by

$$\bar{O}_{(l_e l_h, a, \mathbf{G})(l_e l_h, b, \mathbf{G}')} = \delta(\mathbf{G} - \mathbf{G}') \delta_{L_a, L_b} \frac{(N_a + N_b - 1)!}{(\mathcal{Z}_{l_e l_h, a} + \mathcal{Z}_{l_e l_h, b})^{N_a + N_b}}. \quad (\text{B16})$$

A more detailed derivation of matrix elements of the exciton Hamiltonian by using STOs as the basis function can be found in Refs. [55,56].

-
- [1] Q. H. Wang, K. Kalantar-Zadeh, A. Kis, J. N. Coleman, and M. S. Strano, Electronics and optoelectronics of two-dimensional transition metal dichalcogenides, *Nat. Nanotechnol.* **7**, 699 (2012).
- [2] F. Xia, H. Wang, D. Xiao, M. Dubey, and A. Ramasubramanian, Two-dimensional material nanophotonics, *Nat. Photonics* **8**, 899 (2014).
- [3] K. F. Mak and J. Shan, Photonics and optoelectronics of 2D semiconductor transition metal dichalcogenides, *Nat. Photonics* **10**, 216 (2016).
- [4] J. Xiao, M. Zhao, Y. Wang, and X. Zhang, Excitons in atomically thin 2D semiconductors and their applications, *Nanophotonics* **6**, 1309 (2017).
- [5] T. C. Berkelbach and D. R. Reichman, Optical and excitonic properties of atomically thin transition-metal dichalcogenides *Annu. Rev. Condens. Matter Phys.* **9**, 379 (2018).
- [6] K. Tran, J. Choi, and A. Singh, Moiré and beyond in transition metal dichalcogenide twisted bilayers, *2D Mater.* **8**, 022002 (2021).
- [7] D. M. Kennes, M. Claassen, L. Xian, A. Georges, A. J. Millis, J. Hone, C. R. Dean, D. N. Basov, A. N. Pasupathy, and A. Rubio, Moiré heterostructures as a condensed-matter quantum simulator, *Nat. Phys.* **17**, 155 (2021).
- [8] K. F. Mak and J. Shan, Semiconductor moiré materials, *Nat. Nanotechnol.* **17**, 686 (2022).
- [9] L. Zhang, R. Ni, and Y. Zhou, Controlling quantum phases of electrons and excitons in moiré superlattices, *J. Appl. Phys.* **133**, 080901 (2023).
- [10] L. Du, M. R. Molas, Z. Huang, G. Zhang, F. Wang, and Z. Sun, Moiré photonics and optoelectronics, *Science* **379**, eadg0014 (2023).
- [11] J. Kunstmann, F. Mooshammer, P. Nagler, A. Chaves, F. Stein, N. Paradiso, G. Plechinger, C. Strunk, C. Schüller, G. Seifert, D. R. Reichman, and T. Korn, Momentum-space indirect interlayer excitons in transition-metal dichalcogenide van der Waals heterostructures, *Nat. Phys.* **14**, 801 (2018).
- [12] P. Rivera, H. Yu, K. L. Seyler, N. P. Wilson, W. Yao, and X. Xu, Interlayer valley excitons in heterobilayers of transition metal dichalcogenides, *Nat. Nanotechnol.* **13**, 1004 (2018).
- [13] E. M. Alexeev, D. A. Ruiz-Tijerina, M. Danovich, M. J. Hamer, D. J. Terry, P. K. Nayak, S. Ahn, S. Pak, J. Lee, J. I. Sohn, M. R. Molas, M. Koperski, K. Watanabe, T. Taniguchi, K. S. Novoselov, R. V. Gorbachev, H. S. Shin, V. I. Fal'ko, and A. I. Tartakovskii, Resonantly hybridized excitons in moiré superlattices in van der Waals heterostructures, *Nature (London)* **567**, 81 (2019).
- [14] C. Jin, E. C. Regan, A. Yan, M. I. B. Utama, D. Wang, S. Zhao, Y. Qin, S. Yang, Z. Zheng, S. Shi, K. Watanabe, T. Taniguchi, S. Tongay, A. Zettl, and F. Wang, Observation of moiré excitons in WSe_2/WS_2 heterostructure superlattices, *Nature (London)* **567**, 76 (2019).
- [15] C. Jin, E. C. Regan, D. Wang, M. I. B. Utama, C.-S. Yang, J. Cain, Y. Qin, Y. Shen, Z. Zheng, K. Watanabe, T. Taniguchi, S. Tongay, A. Zettl, and F. Wang, Identification of spin, valley and moiré quasi-angular momentum of interlayer excitons, *Nat. Phys.* **15**, 1140 (2019).
- [16] K. Tran, G. Moody, F. Wu, X. Lu, J. Choi, K. Kim, A. Rai, D. A. Sanchez, J. Quan, A. Singh, J. Embley, A. Zepeda, M. Campbell, T. Autry, T. Taniguchi, K. Watanabe, N. Lu, S. K. Banerjee, K. L. Silverman, S. Kim, E. Tutuc, L. Yang, A. H. MacDonald, and X. Li, Evidence for moiré excitons in van der Waals heterostructures, *Nature (London)* **567**, 71 (2019).
- [17] T. Deilmann, M. Rohlfing, and U. Wurstbauer, Light-matter interaction in van der Waals hetero-structures, *J. Phys.: Condens. Matter* **32**, 333002 (2020).
- [18] Y. Shimazaki, I. Schwartz, K. Watanabe, T. Taniguchi, M. Kroner, and A. Imamoğlu, Strongly correlated electrons and hybrid excitons in a moiré heterostructure, *Nature (London)* **580**, 472 (2020).
- [19] L. Zhang, Z. Zhang, F. Wu, D. Wang, R. Gogna, S. Hou, K. Watanabe, T. Taniguchi, K. Kulkarni, T. Kuo, S. R. Forrest, and H. Deng, Twist-angle dependence of moiré excitons in $\text{WS}_2/\text{MoSe}_2$ heterobilayers, *Nat. Commun.* **11**, 5888 (2020).
- [20] Y. Tang, J. Gu, S. Liu, K. Watanabe, K. F. Mak, and J. Shan, Tuning layer-hybridized moiré excitons by the quantum-confined Stark effect, *Nat. Nanotechnol.* **16**, 52 (2021).
- [21] Y. Jiang, S. Chen, W. Zheng, B. Zheng, and A. Pan, Interlayer exciton formation, relaxation, and transport in TMD van der Waals heterostructures, *Light: Sci. Appl.* **10**, 72 (2021).
- [22] Y. Liu, C. Zeng, J. Yu, J. Zhong, B. Li, Z. Zhang, Z. Liu, Z. M. Wang, A. Pan, and X. Duan, Moiré superlattices and related moiré excitons in twisted van der Waals heterostructures, *Chem. Soc. Rev.* **50**, 6401 (2021).
- [23] N. P. Wilson, W. Yao, J. Shan, and X. Xu, Excitons and emergent quantum phenomena in stacked 2D semiconductors, *Nature* **599**, 383 (2021).
- [24] D. Huang, J. Choi, C.-K. Shih, and X. Li, Excitons in semiconductor moiré superlattices, *Nat. Nanotechnol.* **17**, 227 (2022).
- [25] B.-H. Lin, Y.-C. Chao, I.-T. Hsieh, C.-P. Chuu, C.-J. Lee, F.-H. Chu, L.-S. Lu, W.-T. Hsu, C.-W. Pao, C.-K. Shih, J.-J. Su, and W.-H. Chang, Remarkably deep moiré potential for intralayer excitons in $\text{MoSe}_2/\text{MoS}_2$ twisted heterobilayers, *Nano Lett.* **23**, 1306 (2023).
- [26] A. Chaves, J. G. Azadani, V. O. Özçelik, R. Grassi, and T. Low, Electrical control of excitons in van der Waals heterostructures with type-II band alignment, *Phys. Rev. B* **98**, 121302(R) (2018).
- [27] W.-T. Hsu, B.-H. Lin, L.-S. Lu, M.-H. Lee, M.-W. Chu, L.-J. Li, W. Yao, W.-H. Chang, and C.-K. Shih, Tailoring excitonic states of van der Waals bilayers through stacking configuration band alignment, and valley spin, *Sci. Adv.* **5**, eaax7407 (2019).

- [28] J. Hagel, S. Brem, C. Linderålv, P. Erhart, and E. Malic, Exciton landscape in van der Waals heterostructures, *Phys. Rev. Res.* **3**, 043217 (2021).
- [29] H. Yu, Y. Wang, Q. Tong, X. Xu, and W. Yao, Anomalous light cones and valley optical selection rules of interlayer excitons in twisted heterobilayers, *Phys. Rev. Lett.* **115**, 187002 (2015).
- [30] H. Yu, G.-B. Liu, J. Tang, X. Xu, and W. Yao, Moiré excitons: From programmable quantum emitter arrays to spin-orbit-coupled artificial lattices, *Sci. Adv.* **3**, e1701696 (2017).
- [31] F. Wu, T. Lovorn, and A. H. MacDonald, Topological exciton bands in moiré heterojunctions, *Phys. Rev. Lett.* **118**, 147401 (2017).
- [32] F. Wu, T. Lovorn, and A. H. MacDonald, Theory of optical absorption by interlayer excitons in transition metal dichalcogenide heterobilayers, *Phys. Rev. B* **97**, 035306 (2018).
- [33] M. Danovich, D. A. Ruiz-Tijerina, R. J. Hunt, M. Szytniszewski, N. D. Drummond, and V. I. Fal'ko, Localized interlayer complexes in heterobilayer transition metal dichalcogenides, *Phys. Rev. B* **97**, 195452 (2018).
- [34] D. A. Ruiz-Tijerina and V. I. Fal'ko, Interlayer hybridization and moiré superlattice minibands for electrons and excitons in heterobilayers of transition-metal dichalcogenides, *Phys. Rev. B* **99**, 125424 (2019).
- [35] D. A. Ruiz-Tijerina, I. Soltero, and F. Mireles, Theory of moiré localized excitons in transition metal dichalcogenide heterobilayers, *Phys. Rev. B* **102**, 195403 (2020).
- [36] S. Brem, K.-Q. Lin, R. Gillen, J. M. Bauer, J. Maultzsch, J. M. Lupton, and E. Malic, Hybridized intervalley moiré excitons and flat bands in twisted WSe₂ bilayers, *Nanoscale* **12**, 11088 (2020).
- [37] S. Brem, C. Linderålv, and P. Erhart, and E. Malic, Tunable phases of moiré excitons in van der Waals heterostructures, *Nano Lett.* **20**, 8534 (2020).
- [38] H. Guo, X. Zhang, and G. Lu, Shedding light on moiré excitons: A first-principles perspective, *Sci. Adv.* **6**, eabc5638 (2020).
- [39] J. Choi, M. Florian, A. Steinhoff, D. Erben, K. Tran, D. S. Kim, L. Sun, J. Quan, R. Claassen, S. Majumder, J. A. Hollingsworth, T. Taniguchi, K. Watanabe, K. Ueno, A. Singh, G. Moody, F. Jahnke, and X. Li, Twist angle-dependent interlayer exciton lifetimes in van der Waals heterostructures, *Phys. Rev. Lett.* **126**, 047401 (2021).
- [40] A. Hichri, T. Amand, and S. Jaziri, Resonance energy transfer from moiré-trapped excitons in MoSe₂/WSe₂ heterobilayers to graphene: Dielectric environment effect, *Phys. Rev. Mater.* **5**, 114002 (2021).
- [41] H. Yu and W. Yao, Luminescence anomaly of dipolar valley excitons in homobilayer semiconductor moiré superlattices, *Phys. Rev. X* **11**, 021042 (2021).
- [42] A. Julku, Nonlocal interactions and supersolidity of moiré excitons, *Phys. Rev. B* **106**, 035406 (2022).
- [43] M. H. Naik, E. C. Regan, Z. Zhang, Y.-H. Chan, Z. Li, D. Wang, Y. Yoon, C. S. Ong, W. Zhao, S. Zhao, M. I. B. Utama, B. Gao, X. Wei, M. Sayyad, K. Yumigeta, K. Watanabe, T. Taniguchi, S. Tongay, F. H. da Jornada, F. Wang, and S. G. Louie, Intralayer charge-transfer moiré excitons in van der Waals superlattices, *Nature (London)* **609**, 52 (2022).
- [44] J. Hagel, S. Brem, and E. Malic, Electrical tuning of moiré excitons in MoSe₂ bilayers, *2D Mater.* **10**, 014013 (2023).
- [45] F. Wu, T. Lovorn, E. Tutuc, and A. H. MacDonald, Hubbard model physics in transition metal dichalcogenide moiré bands, *Phys. Rev. Lett.* **121**, 026402 (2018).
- [46] N. S. Rytova, *Vestn. Mosk. Univ. Fiz. Astron.* **3**, 30 (1967).
- [47] L. V. Keldysh, *Pis'ma Zh. Eksp. Teor. Fiz.* **29**, 716 (1979) [*J. Exp. Theor. Phys. Lett.* **29**, 658 (1979)].
- [48] K. S. Thygesen, Calculating excitons, plasmons, and quasiparticles in 2D materials and van der Waals heterostructures, *2D Mater.* **4**, 022004 (2017).
- [49] L. S. R. Cavalcante, A. Chaves, B. Van Duppen, F. M. Peeters, and D. R. Reichman, Electrostatics of electron-hole interactions in van der Waals heterostructures, *Phys. Rev. B* **97**, 125427 (2018).
- [50] M. Van der Donck and F. M. Peeters, Interlayer excitons in transition metal dichalcogenide heterostructures, *Phys. Rev. B* **98**, 115104 (2018).
- [51] F. García Flórez, D. A. Siebbeles, and H. T. C. Stoof, Effects of material thickness and surrounding dielectric medium on Coulomb interactions and two-dimensional excitons, *Phys. Rev. B* **102**, 125303 (2020).
- [52] H. E. Hannachi, D. Elmaghraoui, and S. Jaziri, Moiré interlayer exciton relative and center of mass motions coupling. Effect on 1s-*np* interlayer exciton THz transitions, *Eur. Phys. J. Plus* **138**, 396 (2023).
- [53] J.-Z. Zhang and J.-Z. Ma, Two-dimensional excitons in monolayer transition metal dichalcogenides from radial equation and variational calculations, *J. Phys.: Condens. Matter* **31**, 105702 (2019).
- [54] S. Wu, L. Cheng, and Q. Wang, Exciton states and absorption spectra in freestanding monolayer transition metal dichalcogenides: A variationally optimized diagonalization method, *Phys. Rev. B* **100**, 115430 (2019).
- [55] Y.-W. Chang and Y.-C. Chang, Variationally optimized orbital approach to trions in two-dimensional materials, *J. Chem. Phys.* **155**, 024110 (2021).
- [56] Y.-W. Chang and Y.-C. Chang, Theory of magnetic-field effect on trions in two-dimensional materials, *J. Chem. Phys.* **157**, 044104 (2022).
- [57] M. Goryca, J. Li, A. V. Stier, T. Taniguchi, K. Watanabe, E. Courtade, S. Shree, C. Robert, B. Urbaszek, X. Marie and S. A. Crooker, Revealing exciton masses and dielectric properties of monolayer semiconductors with high magnetic fields, *Nat. Commun.* **10**, 4172 (2019).
- [58] J. A. Wilson and A. D. Yoffe, The transition metal dichalcogenides discussion and interpretation of the observed optical, electrical and structural properties, *Adv. Phys.* **18**, 193 (1969).
- [59] C. Zhang, C. Gong, Y. Nie, K.-A. Min, C. Liang, Y. J. Oh, H. Zhang, W. Wang, S. Hong, L. Colombo, R. M. Wallace, and K. Cho, Systematic study of electronic structure and band alignment of monolayer transition metal dichalcogenides in van der Waals heterostructures, *2D Mater.* **4**, 015026 (2016).
- [60] A. Kormányos, G. Burkard, M. Gmitra, J. Fabian, V. Zólyomi, N. D. Drummond, and V. Falko, $\mathbf{k} \cdot \mathbf{p}$ theory for two-dimensional transition metal dichalcogenide semiconductors, *2D Mater.* **2**, 022001 (2015).
- [61] H. Rydberg, M. Dion, N. Jacobson, E. Schröder, P. Hyldgaard, S. I. Simak, D. C. Langreth, and B. I. Lundqvist, Van der Waals density functional for layered structures, *Phys. Rev. Lett.* **91**, 126402 (2003).

- [62] S. Shabani, D. Halbertal, W. Wu, M. Chen, S. Liu, J. Hone, W. Yao, D. N. Basov, X. Zhu, and A. N. Pasupathy, Deep moiré potentials in twisted transition metal dichalcogenide bilayers, *Nat. Phys.* **17**, 720 (2021).
- [63] H. Zheng, D. Zhai, and W. Yao, Twist versus heterostrain control of optical properties of moiré exciton minibands, *2D Mater.* **8**, 044016 (2021).
- [64] H. Zheng, D. Zhai, and W. Yao, Anomalous magneto-optical response and chiral interface of dipolar excitons at twisted valleys, *Nano Lett.* **22**, 5466 (2022).
- [65] J. Schwinger, L. L. DeRaad, Jr., K. Milton, and W.-Y. Tsai, *Classical Electrodynamics* (Westview Press, Perseus Books, Reading, Massachusetts, USA, 1998).